



Simon Prato

Numerical Investigation of TEM Cells and Antenna Coupling

Master Thesis

Studies: Electrical Engineering

submitted to

Technical University of Graz

Supervisor

Dr. Thomas Bauernfeind



Graz, August 2024

Abstract

Contents

1	Introduction	1
2	Theoretical Basics	1
2.1	Dipoles	1
2.1.1	Electric Dipoles	1
2.1.2	Magnetic Dipoles	3
2.1.3	Crossed Dipoles	4
2.2	Finite Element Method	4
2.2.1	General Idea	4
2.2.2	Dividing a computational domain into finite elements	4
2.2.3	Solving the differential equation	6
2.2.4	Adaptive solution process	7
2.3	Lorentz Reciprocity Theorem	8
2.4	Green's Function	9
2.5	Numerical Investigation of Propagating Modes in TEM Cells	10
2.5.1	Mathematical derivation	10
2.5.2	Modes in TEM cell	11
2.6	Electrically Small Radiating Sources in TEM Cells	15
2.7	Shielding	17
2.7.1	ASTM ES7-83 Method	19
2.7.2	Dual TEM cell	20
3	Antennas	21
3.1	Antennas to Investigate	21
3.1.1	IFA	21
3.1.2	Center fed monopole antenna	21
3.2	Crossed dipole antenna	21
4	Simulations	22
4.1	Antennas	22
4.1.1	Inverted F-antenna	22
4.1.2	Center Fed Monopole Antenna	29
4.1.3	Monopole Antenna	32
4.1.4	Loop antenna	34
4.1.5	Offset of source antennas and eddy currents	39
4.2	Dipole Moments	39
4.2.1	Orientation and position in TEM Cell	41
4.2.2	Combining dipole moments with antennas	42
4.3	Shielding Simulations	42
4.3.1	Shielding effectiveness of graphite	42
4.3.2	Shield effectiveness of FR4	42
4.3.3	Dual TEM Cell	42

List of Figures

1	Electric dipole	2
2	Magnetic dipole	3
3	Tetrahedron with points on the edge and vertices.	5
4	Face of the finite element with unknowns	6
5	Adaptive solution process	8
6	Cross section of the TEM cell	13
7	Propagation of TEM, TE ₀₁ and TE ₁₀ modes in TEM cell	14
8	Transversal electric fields in cross section of TEM cell	14
9	Normalized e-field distribution along z-axis at center of septum	17
10	Incident, reflected and transmitted electric fields due to interaction with shielding material	17
12	Dual TEM cell with aperture	21
13	Inverted F-antenna used in the simulation	22
14	S-parameter describing coupling of antenna to waveport 1	22
15	Phase of S-parameters from antenna to waveport 1 and 2	24
16	Dipole moments and measurement point of $e_{0,z}$ in TEM cell	25
17	Dipole moments over frequency	26
18	Output power and electric field over frequency	27
19	Phase of S-parameters from rotated antenna to waveport 1 and 2	27
20	Dipole moments of rotated antenna	28
21	Center fed monopole antenna used in simulation	29
22	S-parameter describing coupling of antenna to waveport 1	29
23	Phase of S-parameters from antenna to waveport 1 and 2	30
24	Dipole moments over frequency	31
25	Dipole moments of CFM antenna rotated by 79°	31
26	Dipole moments of the monopole antenna	32
27	Current surface density at 550 MHz	32
28	Current surface density at 550 MHz with offset	33
29	Feed current over frequency of monopole antenna	33
30	Dipole moments of loop antenna	34
31	Surface current density at 550 MHz	34
32	Surface current density at 550 MHz with offset	35
33	Surface current density at 550 MHz with rotated antenna	35
34	Surface current density at 550 MHz with offset and rotated antenna	36
35	Charge density distribution in current loop antenna	36
36	Current density distribution in current loop antenna	36
37	Electric near field in current loop antenna	36
38	Magnetic near field in current loop antenna	36
39	Voltage drop at feed point of current loop antenna	37
40	Current consumption at feed point of current loop antenna	37
41	Power consumption of the current loop antenna	38
42	Total power distribution in the system	38
43	CFM S11 sweep with rotation angle stepping	40
44	Center fed monopole antenna coupling dependence on offset (Delete after) .	40

List of Tables

1	Forward transmission coefficients	43
---	---	----

1 Introduction

2 Theoretical Basics

2.1 Dipoles

Modeling the electromagnetic radiation from antennas is a challenging task. Employing magnetic and electric dipoles is an effective approach, particularly for electrically small antennas. They are defined as antennas with dimensions much less than one-tenth of the wavelength ($<< \frac{\lambda}{10}$)[2]. By calculating the respective dipole moments, the coupling between antennas and TEM cells can be numerically estimated. This section provides a brief introduction to the underlying theory of this concept.

2.1.1 Electric Dipoles

An electric dipole is often described as two tiny charged metal spheres, which are connected with a linear and thin wire [8] or simply as an T-antenna containing charged capacitor-plates at the ends of the wire [2]. The distance d between those charges is very short compared to the wavelength ($d << \lambda$). The electric dipole moment \mathbf{p} is defined by the product of charges and their separation distance, as expressed in Equation 1[2, 11].

$$\mathbf{p} = \iiint \mathbf{x}' \rho(\mathbf{x}') d^3x' \quad (1)$$

Figure 1 demonstrates a simple center-fed wire antenna with a narrow gap as the feedpoint. Since the wire is electrically small and very thin, it can be accurately modeled as an electric dipole [8, 11]. A current I_0 is injected at the feedpoint, which linearly drops to zero along the antenna arms, as described by Equation 2[11].

$$I(z) = I_0 \left(1 - \frac{2|z|}{d} \right) \quad (2)$$

Charge accumulates along the antenna's arms and is expressed as a charge per unit length ρ' . The charge distribution ρ' is derived by the continuity equation in frequency domain, as shown in Equation 3. It is uniformly distributed along each antenna arm [8, 11].

$$\rho' = \pm \frac{d}{dz} \frac{iI(z)}{\omega} = \pm \frac{2iI_0}{\omega d} \quad (3)$$

Knowing the charge distribution ρ' enables the calculation of the electric dipole moment \mathbf{p} using Equation 1. This results in Equation 4. The electric dipole moment \mathbf{p} is parallel to the antenna's arms and points in the z-direction [8][11].

$$\mathbf{p} = \int_{-\frac{d}{2}}^{\frac{d}{2}} z \rho'(z) dz \cdot \mathbf{e}_z = \frac{iI_0 d}{2\omega} \quad (4)$$

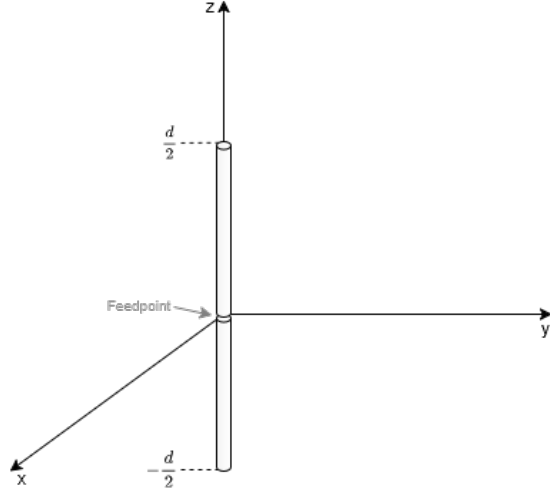


Figure 1: Electric dipole

Next, the vector potential \mathbf{A} is determined. It is generally defined in Equation 5[2][11].

$$\mathbf{A}(\mathbf{x}) = \frac{\mu}{4\pi} \frac{e^{ikr}}{r} \iiint \mathbf{J}(\mathbf{x}') d^3x' \quad (5)$$

In the case of an electric dipole, the calculations of the vector potential \mathbf{A} simplifies to Equation 6[11].

$$\mathbf{A}(\mathbf{x}) = -\frac{i\mu_0\omega}{4\pi} \mathbf{p} \frac{e^{ikr}}{r} \quad (6)$$

Any other field quantities can be derived out of the vector potential \mathbf{A} , such as the electric field strength \mathbf{E} and magnetic field strength \mathbf{H} . Equation 7 expresses their relation [2].

$$\mathbf{H} = \hat{a}_\phi \frac{1}{\mu r} \left[\frac{\partial}{\partial r} (r A_\theta) - \frac{\partial A_r}{\partial \theta} \right] \quad (7a)$$

$$\mathbf{E} = -i\omega \mathbf{A} - i \frac{1}{\omega \mu \epsilon} \nabla (\nabla \cdot \mathbf{A}) \quad (7b)$$

The power radiated by an antenna is determined from the time-averaged Poynting vector $\langle \mathbf{S} \rangle$. Equation 8 defines this quantity, where only the real part is relevant, since it represents the actual radiated power [2].

$$\langle \mathbf{S} \rangle = \frac{1}{2} \Re \{ \mathbf{E} \times \mathbf{H}^* \} \quad (8)$$

By integrating the time-averaged Poynting vector $\langle \mathbf{S} \rangle$ over a closed surface, the radiated power P_{rad} is determined. The real part of the power is independent of the integrated

surface, and in case of an electric dipole is expressed as Equation 9. The radiated power increases with the frequency squared, as the antenna becomes more efficient. This relation holds, as long as the antenna is electrically small.

$$P_{\text{rad}} = \frac{c^2 Z_0 k^4}{12\pi} |\mathbf{p}|^2 \quad (9)$$

The electric dipole described in this section approximate the real behavior of electrically short antennas. However, special care must be taken of the excitation method and shape, as it influences the results heavily [11]. Additionally, any antenna investigated through this method must remain as small as possible compared to the wavelength λ , to reduce any analytical approximation errors.

2.1.2 Magnetic Dipoles

The magnetic dipole is modeled as a current loop with radius b , whose axis is perpendicular to the plane of the loop. Its radiated fields are analogous to those of an electric dipole, with the electric and magnetic fields interchanged [2]. Figure 2 shows a magnetic dipole.

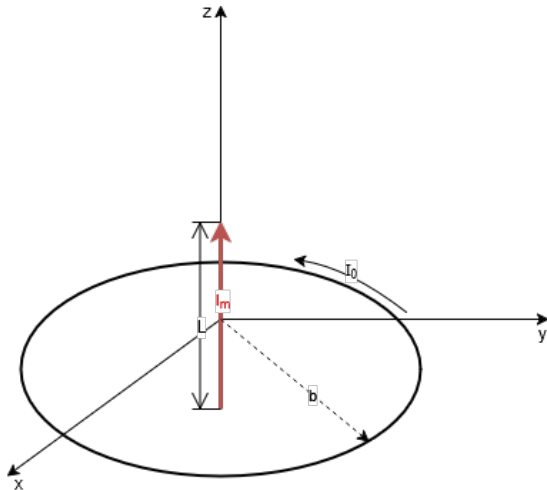


Figure 2: Magnetic dipole

The magnetic dipole moment is given by Equation 10.

$$\mathbf{m} = \frac{1}{2} \int (\mathbf{x} \times \mathbf{J}) d^3x \quad (10)$$

A magnetic dipole can be represented with a current loop, or a magnetic current along a straight path. Equation 11 shows the mathematical relation between these two [2].

$$I_m L = i S \omega \mu_0 I_0 \quad (11)$$

Balanis Book chapter: image theory of dipoles. Additionally, describe electric field which increases quadratically with frequency, leading to an increase in dipole moment. Griffiths.

I_m is the magnetic current with the unit V. The area S of the loop is calculated by $b^2\pi$. I_0 is the electric current with the unit A flowing through the loop, and μ_0 is the permeability of free space.

Add fields and radiation power formulas, if it is needed later

2.1.3 Crossed Dipoles

Crossed dipoles can generate a wide variety of radiation patterns. Supposed two dipoles are placed perpendicular to each other and fed 90° out of phase, an omnidirectional radiation pattern is created [25]. If the equivalent dipoles of an EUT represents such two dipoles, any mode which can propagate in the TEM cell will do so, and therefore influence the measurement result. It is therefore not only important to know which dipoles there are representing the EUT, but also what phase and magnitude they have. Meaning that not only the dipoles aligned with the TEM mode alone influence the result.

Write

Dipoles next to conducting planes (balanis, collin)

2.2 Finite Element Method

2.2.1 General Idea

Problems involving the calculations of electromagnetic fields are often cumbersome and difficult to solve. This is due to the need of solving differential equations describing these fields over a computational domain, which is not possible with a computer in this sense. The simulation software Ansys HFSS (High Frequency Simulation Software) aims to provide a solution. This software is used for the simulations in section 4, hence it is described in this following, dedicated section.

HFSS uses a numerical technique, namely the Finite Element Method (FEM). The general idea of FEM after Rayleigh-Ritz-Galerkin is to choose a number of basis functions. The goal is to find a linear combination of these basis functions, so that the differential equation is satisfied as closely as possible. This turns the problem of solving a differential equation into a system of algebraic equations, which the computer can process. There is always a set of basis functions which enable the calculation to converge to the real solution. However, the number of basis functions used in the domain is limited, due to reasons of computability [24].

FEM therefore divides the domain into finite elements, i.e. smaller pieces. Then, within each piece, such a basis function is assigned. A linear combination of these basis functions are found, which satisfy the differential equations. In region where the approximating solution has a high degree of error, the accuracy may be increased by further subdividing the finite elements. This is repeated, until the error falls below a certain threshold, and a precise solution is derived.

2.2.2 Dividing a computational domain into finite elements

The differential equation to be solved is shown in Equation 12, where ϵ_r is the relative permeability and μ_r is the relative permeability of the material. The variable k_0 is the wave number of free space and equals $k_0 = \omega\sqrt{\epsilon_0\mu_0}$. [5, 17, 4].

$$\nabla \times \left(\frac{1}{\mu_r} \nabla \times \mathbf{E} \right) - k_0^2 \epsilon_r \mathbf{E} = 0 \quad \text{in } \Omega \quad (12)$$

This equation is solved in a computational domain Ω . This computational domain is divided into finite elements, called a mesh. Each node in this mesh has polynomial functions assigned, which are weighted to approximate the real solution. It has been proven that tetrahedral finite elements are best suited for this task, as they are geometrically flexible and make the definition of complete polynomial approximation functions possible [22]. Ansys HFSS uses a adaptive finite element mesh generator, which automatically provides a mesh for a given 3-dimensional construction. The Delaunay tessellation for three-dimensions is used for generating a mesh. It efficiently creates a mesh from objects of arbitrary shapes. Any boundary condition can be added recursively to the mesh. At the heart of this algorithm lies the property, that the circumsphere of an tetrahedra's vertices may not contain other tetrahedra's vertices.

Figure 3 shows one of such tetrahedrons. At the edge points, the components of the field which are normal to the respective edge and tangential to the face of the element is stored. At the vertex points, the component of a field which are tangential to the edges are stored. The value of the field at any midpoint is derived through interpolation from the node values. The basis function is used for interpolation.

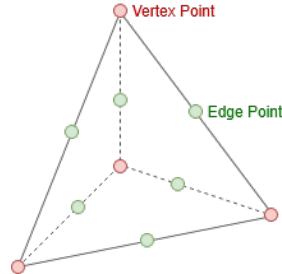


Figure 3: Tetrahedron with points on the edge and vertices.

Because of the way how the fields are stored in the tetrahedra, they are called tangential vector finite elements. Their advantage is that tangential components of fields can be forced to be equal among adjacent tetrahedra at the boundary. For example, an electric field stored at a vertex point must point in the direction along one of the edges, therefore it is tangential to the element. An adjacent element then has the same tangential electric field imposed at this node, leading to a continuous tangential electric field, therefore satisfying the boundary conditions implied by the Maxwell equation automatically. Furthermore, any Dirichlet boundary conditions can easily be set along the edges. [17].

The finite element is described as Equation 13, where $L_2(\Omega)$ is a set of square integrable functions and P_1 a set of piecewise linear functions in the discretized domain Ω [18]. The vector fields at the vertices are given as u . $D(\Omega)$ is a set of divergence free functions. The vectors u used in the finite element therefore

- are continuous in the normal direction.

- are square integrable.
- have a curl describable by piecewise linear functions.

$$H_1^{(\text{dim}=3)}(\text{curl}) = \left\{ \mathbf{u} \mid \mathbf{u} \in [L_2(\Omega)]^3, \nabla \times \mathbf{u} \in [P_1(\Omega)]^3 \cap D(\Omega) \right\} \quad (13)$$

Figure 4 shows the finite element with the unknowns marked at each point. For reasons of simplicity, only the face is shown. The variables u_i^j and u_j^i are imposed across element boundaries, therefore guaranteeing tangential continuity at boundaries. Additionally, they inherently defined a linear polynomial, meaning that they describe a gradient of the field along this edge. Equation 14 describes this relation mathematically, where \mathbf{t}_{ij} is the unit vector tangentially to the edge from node i to node j and l_{ij} is the length of this edge.

$$\mathbf{u} \cdot \mathbf{t}_{ij} = \frac{1}{l_{ij}} (u_i^j - u_j^i) \quad (14)$$

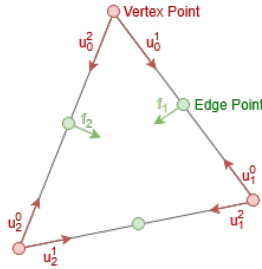


Figure 4: Face of the finite element with unknowns

Two facial unknowns f_1 and f_2 are added to two of the three edge points at one face. Contrary to the variables u_i^j , the facial unknowns f_i are only assigned locally at each element and do not cross boundaries. The purpose of the facial unknowns f is to provide a quadratic polynomial for the field component normal to the edges. This will lead to a linear approximation for the curl of the unknown vector field $\nabla \times \mathbf{u}$, providing sufficient accuracy. The overall vector field of this element is then calculated by a superposition of all nodes' vector attributions.

2.2.3 Solving the differential equation

A testing function \mathbf{W}_n is defined, which is multiplied to Equation 12. Integrating over the whole test volume then leads to Equation 15. This yields N equations, with $n = 1, 2, \dots, N$, for each finite element in the domain Ω . This is a common procedure in FEM, and it works through orthogonalization of the residual of Equation 12 with respect to the function \mathbf{W}_n . This means the new goal of the solution is to minimize the residual by making \mathbf{W}_n as orthogonal as possible [20].

$$\int_{\Omega} \left(\mathbf{W}_n \cdot \nabla \times \left(\frac{1}{\mu_r} \nabla \times \mathbf{E} \right) - k_0^2 \epsilon_r \mathbf{W}_n \cdot \mathbf{E} \right) dV = 0 \quad (15)$$

Using the vector identity $\nabla \cdot (\mathbf{a} \times \mathbf{b}) = (\nabla \times \mathbf{a}) \cdot \mathbf{b} - \mathbf{a} \cdot (\nabla \times \mathbf{b})$ on Equation 15 provides a weak form of the equation, meaning a form of the original partial differential equation, which does not contain all original derivatives [5, 4]. Additionally, boundary terms come into play, as seen in the right hand side of the resulting Equation 16. The usefulness in this step has been described as lowering the highest-order derivative, therefore the approximating functions need to guarantee continuity of value, not of slope [10]. Another explanation is the possibility of incorporation of Neumann boundary conditions [20].

$$\int_{\Omega} \left[(\nabla \times \mathbf{W}_n) \cdot \frac{1}{\mu_r} \nabla \times \mathbf{E} - k_0^2 \epsilon_r \mathbf{W}_n \cdot \mathbf{E} \right] dV = \oint_{\partial\Omega} \underbrace{\left(\mathbf{W}_n \times \frac{1}{\mu_r} \nabla \times \mathbf{E} \right)}_{\text{Boundary term}} \cdot d\mathbf{S} \quad (16)$$

Next, the electric field \mathbf{E} is represented by a superposition of basis functions. When applying Galerkin's method, the basis functions are equal to the test functions W_n . Equation 17 demonstrates the sum of the basis functions, which are weighted with the variable x_m . These variables x for all elements have to be solved, to find the electric field \mathbf{E} over the whole domain. The FEM has therefore reduced the initial wave equation in Equation 12 to a simple linear matrix equation $Ax = b$, where A is a known $N \times N$ matrix, b contains port excitations and x is the unknown. Ideally, the basis functions are defined to be zero outside of their adjacent elements. This will result to zero for all entries in the matrix, where the test and basis function do not overlap. Therefore, the matrix is sparse, and will be solved much faster. In the end, other electromagnetic quantities can all be derived through the electric field.

$$\mathbf{E} = \sum_m^N x_m \mathbf{W}_n \quad (17)$$

Equation 18 shows what the matrix then looks like. Some manipulation on the boundary term have been made, so that it contains the surface impedance Z_s . The surface impedance defines the ratio of the electric field to the magnetic field on the boundary region. Furthermore, it contains the free space, which equals $\eta_0 \approx 377 \Omega$.

$$A_{ij} = \int_{\Omega} \nabla \times \mathbf{W}_i \frac{1}{\mu_r} \nabla \times \mathbf{W}_j dV - k_0^2 \int_{\Omega} \mathbf{W}_i \epsilon_r \mathbf{W}_j dV + ik_0 \left(\frac{\eta_0}{Z_s} \right) \oint_{\partial\Omega} \mathbf{n} \times \mathbf{W}_i \cdot \mathbf{n} \times \mathbf{W}_j d\mathbf{S} \quad (18)$$

2.2.4 Adaptive solution process

Each finite element therefore has a solved electric field assigned, which should approximate the real solution as closely as possible. To determine the error for each element, Equation 12 is evaluated. The elements with the highest residuals contain the largest deviation from the real result, meaning they have a large degree of error. Region in the mesh with large degrees of errors are refined, i.e. the tetrahedral finite elements are split into smaller ones. This allows the FEM solver to recalculate the fields in this region with

higher precision, leading to a smaller residual. Consequently, the finite elements represent the fields more accurately, due to a smaller element size and higher resolution [3]. An additional method is increasing the order of the polynomial basis functions of elements with low degree of accuracy.

$$\nabla \times \left(\frac{1}{\mu_r} \nabla \times \mathbf{E}_{\text{solved}} \right) - k_0^2 \epsilon_r \mathbf{E}_{\text{solved}} = \text{residual} \quad (19)$$

To determine when the iterative refinement process is done and the solution good enough, some kind of threshold must be defined. One possibility is the Max ΔS parameter. It is compared to the difference of S-parameters of the defined excitation ports over two iterations. If, after a mesh refinement, the S-parameters of the ports do not significantly change anymore, meaning change less than Max ΔS , then the iterative process can be considered done. This described iterative process is shown in Figure 5.

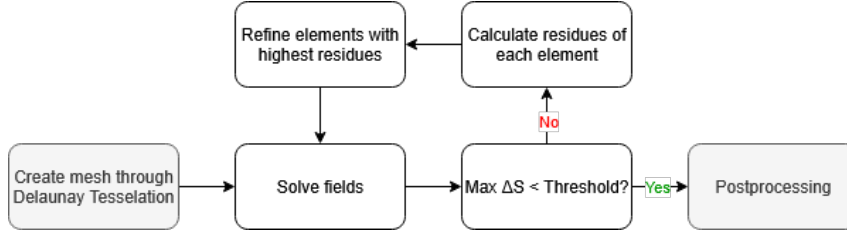


Figure 5: Adaptive solution process

Short HFSS introduction with boundary conditions, ports and modal and terminal solutions?

2.3 Lorentz Reciprocity Theorem

The Lorentz reciprocity theorem proves to be very useful, hence it is summarized here. It states that any two fields $\mathbf{E}_1, \mathbf{H}_1$ and $\mathbf{E}_2, \mathbf{H}_2$, which are of the same frequency and in linear and isotropic media, can be expressed by its differential form in Equation 20 [2, 6]. Here, \mathbf{J} describes the electric current density with the unit $\frac{\text{A}}{\text{m}^2}$ and \mathbf{M} the magnetic current density with the unit $\frac{\text{V}}{\text{m}^2}$. They act as sources, exciting the electric and magnetic fields \mathbf{E} and \mathbf{H} . The theorem says, that under the previously described conditions, any source and response can be locally interchanged, and the results would remain the same.

$$-\nabla \cdot (\mathbf{E}_1 \times \mathbf{H}_2 - \mathbf{E}_2 \times \mathbf{H}_1) = \mathbf{E}_1 \cdot \mathbf{J}_2 + \mathbf{H}_2 \cdot \mathbf{M}_1 - \mathbf{E}_2 \cdot \mathbf{J}_1 - \mathbf{H}_1 \cdot \mathbf{M}_2 \quad (20)$$

By taking a volume integral of both sides of Equation 20 and using the divergence theorem, Equation 21 emerges [2, 6].

$$\oint\oint (\mathbf{E}_1 \times \mathbf{H}_2 - \mathbf{E}_2 \times \mathbf{H}_1) \cdot dS \mathbf{n} = \iiint \mathbf{E}_1 \cdot \mathbf{J}_2 + \mathbf{H}_2 \cdot \mathbf{M}_1 - \mathbf{E}_2 \cdot \mathbf{J}_1 - \mathbf{H}_1 \cdot \mathbf{M}_2 \cdot dV \quad (21)$$

If there aren't any sources present, meaning that $\mathbf{J}_1 = \mathbf{J}_2 = \mathbf{M}_1 = \mathbf{M}_2 = 0$, the Lorentz reciprocity theorem simplifies to Equation 22 [2, 19]. This is especially useful for free wave propagation of antennas.

$$-\nabla \cdot (\mathbf{E}_1 \times \mathbf{H}_2 - \mathbf{E}_2 \times \mathbf{H}_1) = 0 \quad (22)$$

Another application arises when investigating a volume V confined by a perfectly conducting surface S , through which two linear current densities \mathbf{J}_1 and \mathbf{J}_2 flow. Because $\mathbf{n} \times \mathbf{E}_1 = \mathbf{n} \times \mathbf{E}_2 = 0$ along the surface S , the surface integral in Equation 21 equals zero, and Equation 23 arises. This is the Rayleigh-Carson form of the Lorentz reciprocity theorem and is particularly useful for deriving waveguide modes and constructing the respective fields [6].

$$\mathbf{E}_1 \cdot \mathbf{J}_2 = \mathbf{E}_2 \cdot \mathbf{J}_1 \quad (23)$$

2.4 Green's Function

Green's function describes the response of a linear differential operator L to a point source, described with a delta-function δ . The general form is shown in Equation 24.

$$LG(\mathbf{x}, \mathbf{x}') = \delta(\mathbf{x} - \mathbf{x}') \quad (24)$$

Once Equation 24 is solved and the Green's function G of this specific operator is known, it can be used to solve any function, like $u(\mathbf{x})$ in Equation 25a, on which this operator is used on, by superposition. The resulting Equation 25b solves for $u(\mathbf{x})$ by using a convolution integral with the Green's function and the source function $f(\mathbf{x})$.

$$Lu(\mathbf{x}) = f(\mathbf{x}) \quad (25a)$$

$$u(\mathbf{x}) = \int G(\mathbf{x}, \mathbf{x}') f(\mathbf{x}') d\mathbf{x}' \quad (25b)$$

For example, it is commonly used to solve equations containing the Nabla operator ∇ in electrostatics. Equation 26a and Equation 26b demonstrate how the scalar potential ϕ can be calculated with point sources in space ρ just by knowing the Green's function of the Nabla operator, which is $G(\mathbf{x}, \mathbf{x}') = \frac{1}{4\pi|\mathbf{x}-\mathbf{x}'|}$.

$$\nabla \phi = -\frac{\rho}{\epsilon_0} \quad (26a)$$

$$\phi(\mathbf{x}) = \frac{1}{4\pi\epsilon_0} \iiint_V \frac{\rho(\mathbf{x}')}{|\mathbf{x} - \mathbf{x}'|} dV' \quad (26b)$$

When boundary conditions are present, the Green's function may be modified to make the boundary condition vanish. Same goes for the dyadic Green's function, where the boundary condition are considered to create a taylored Green's function. This enables an expansion of the fields in a waveguide excited by an internal source. The perfectly conducting surfaces of the waveguides mirror the source infinitely often. Therefore, the

Green's function may be represented by a series of these mirror sources. In practice, these calculations are cumbersome, and only the most significant parts of the series are computed [6].

write about dyadic green's function, which just maps the coordinates to each other. More about that in Collin and Balanis

2.5 Numerical Investigation of Propagating Modes in TEM Cells

2.5.1 Mathematical derivation

Any electromagnetic field distribution in a waveguide can be represented by an infinite series of normal modes. Equation 27 shows that each mode is orthogonal to each other, with \mathbf{e}_n^\pm and \mathbf{h}_n^\pm being the function vectors of the electric and magnetic field in transverse direction [6]. A coupling between the modes only occurs due to geometric changes of the waveguide. Additionally, each mode is normalized to \sqrt{W} , shown by Equation 28. Only the transverse fields are investigated in these Equations, because they carry power along the waveguide, opposed to the fields in the propagation direction.

$$\iint \mathbf{e}_n^\pm \times \mathbf{h}_m^\pm dS \mathbf{n} = 0 \quad \text{if } n \neq m \quad (27)$$

$$\iint \mathbf{e}_n^\pm \times \mathbf{h}_n^\pm dS \mathbf{n} = 1 \quad (28)$$

The radiated fields can be described by a summation of normal modes, as in Equation 29 and Equation 30. The coefficients of these modes are straightforward to calculate, due to Lorentz Reciprocity Theorem, if the waveguide's walls are perfectly conducting. Ideally, any higher order mode than the first TEM mode will be suppressed, and the calculation simplifies to $n = 0$. Additionally, it is assumed that the source is electrically small, which makes it possible to represent it with dipoles, further simplifying the equations [14].

$$\mathbf{E}^\pm = \sum_n a_n \mathbf{E}_n^\pm \quad (29)$$

$$\mathbf{H}^\pm = \sum_n a_n \mathbf{H}_n^\pm \quad (30)$$

Suppose a current source \mathbf{J}_1 excites a waveguide (as is the case with the dipoles in the TEM cell). Normally, such a current source would be driven with external fields, but for the sake of the argument, they are ignored. Only \mathbf{E} and \mathbf{H} are considered, which are the fields radiated by \mathbf{J}_1 . Additionally, \mathbf{E}_n^\pm and \mathbf{H}_n^\pm are the resulting waveguide fields, with the signs indicating the direction of propagation. Take Equation 21 and set $\mathbf{J}_2 = \mathbf{M}_1 = \mathbf{M}_2 = 0$. Now, only the current source \mathbf{J}_1 remains, and the Equation 31 emerges.

$$\iint_S (\mathbf{E}_n^\pm \times \mathbf{H} - \mathbf{E} \times \mathbf{H}_n^\pm) \cdot d\mathbf{S} = \iiint \mathbf{J}_1 \cdot \mathbf{E}_n^\pm dV \quad (31)$$

In case of the TEM cell, it is desirable that only the TEM mode is propagating, and that the source is represented by a dipole. Considering an electric dipole, therefore, the

Equation 32 arises. In this equation, the wave amplitudes a and b are given through the surface integral in the Lorentz Reciprocity theorem, with a being the wave going to the left side, and b to the other. The electric dipole moment \mathbf{e}_m is given by the current \mathbf{J} flowing through the infinitesimal wire. Note that only the electric field of TEM wave propagation is considered. In reality, more modes may propagate, for which the electric field must be replaced by the superposition of normal modes as in Equation 29.

$$\begin{pmatrix} a \\ b \end{pmatrix} = -\frac{1}{2}\mathbf{m}_e \cdot \mathbf{E}^\pm \quad (32)$$

$E_n^\pm?$

If this arbitrary current distribution forms an infinitesimal loop, the source can be represented by a magnetic dipole. This leads to Equation 33. The requirement for this formulation to work, is that the magnetic fields \mathbf{H}^\pm does not change over the loop area, i.e. the loop is electrically small [6, 23].

$$\begin{aligned} \begin{pmatrix} a \\ b \end{pmatrix} &= -\oint_C \mathbf{E}^\pm dl \\ &= -\iint_{S_0} \nabla \times \mathbf{E}^\pm d\mathbf{S} \\ &= i\omega\mu_0 \iint_{S_0} \mathbf{H}^\pm \cdot d\mathbf{S} \\ &= i\omega\mu_0 \mathbf{m}_m \mathbf{H}^\pm \end{aligned} \quad (33)$$

If there are several modes propagating, it is useful to find the coefficients of the modes a_n and b_n in Equation 29 and Equation 30. In this case, the orthogonality property in Equation 27 is used to derive Equation 34a and Equation 34b [6]. The wire is described by a curve C , and the tangential vector $\boldsymbol{\tau}$ is used to integrate along this curve.

$$2a_n = -\int_C \boldsymbol{\tau} \cdot \mathbf{E}_n^- dl \quad (34a)$$

$$2b_n = \int_C \boldsymbol{\tau} \cdot \mathbf{E}_n^+ dl \quad (34b)$$

2.5.2 Modes in TEM cell

A TEM cell is often used for EMC test specifications, as it enables the propagation of TEM waves, which resemble planar free-space waves. Additionally, it shields the waves from radiating to the sides, for which it has a clear advantage to a stripline [9, 12]. A simple rectangular waveguide cannot be used for this application. Assuming that a monochromatic wave traveling down the waveguide, the waves will propagate without dampening only at a certain angle of reflection on the perfectly conducting surface. A

short mathematical proof can be shown here, using Maxwell's equation. It shows that the electric and magnetic fields in direction of propagation cannot both be zero.

$$\mathbf{E} = (E_{0,x} \cdot \mathbf{e}_x + E_{0,y} \cdot \mathbf{e}_y + E_{0,z} \cdot \mathbf{e}_z) e^{i(\omega t - kz)} \quad (35)$$

$$\mathbf{H} = (H_{0,x} \cdot \mathbf{e}_x + H_{0,y} \cdot \mathbf{e}_y + H_{0,z} \cdot \mathbf{e}_z) e^{i(\omega t - kz)} \quad (36)$$

$$\nabla \times \mathbf{E} = \begin{pmatrix} \frac{d}{dy} E_z - ik E_y \\ ik E_x - \frac{d}{dx} E_z \\ \frac{d}{dx} E_y - \frac{d}{dy} E_x \end{pmatrix} = \begin{pmatrix} -i\omega B_x \\ -i\omega B_y \\ -i\omega B_z \end{pmatrix} \quad (37)$$

$$\nabla \times \mathbf{B} = \begin{pmatrix} \frac{d}{dy} B_z - ik B_y \\ ik B_x - \frac{d}{dx} B_z \\ \frac{d}{dx} B_y - \frac{d}{dy} B_x \end{pmatrix} = \begin{pmatrix} \frac{i\omega}{\mu\epsilon} E_x \\ \frac{i\omega}{\mu\epsilon} E_y \\ \frac{i\omega}{\mu\epsilon} E_z \end{pmatrix} \quad (38)$$

If E_z and B_z , the fields in direction of propagation, were both zero, then the change of the transverse fields would be constantly zero, and because of the boundary conditions, all transverse fields would be zero. Equation 39 shows Gauss' law and Equation 40 Faraday's law if $E_z = B_z = 0$, from which the unchanging transverse electric field can be derived.

$$\frac{d}{dx} E_x + \frac{d}{dy} E_y = 0 \quad \text{Derived out of Gauss' law} \quad (39)$$

$$\frac{d}{dy} E_x - \frac{d}{dx} E_y = 0 \quad \text{Derived out of Faraday's law} \quad (40)$$

A TEM cell solves this problem, by having a gap between the septum and the side walls. Essentially, it can be considered as two rectangular waveguides with apertures on the sides. Those apertures allow perturbations of the electromagnetic fields between them. The boundary conditions of the Laplace equation now changed due to the gaps. The Green's function may be calculated of the new construction, now considering the boundary conditions at the gaps, which must be the same for both waveguides (to prevent discontinuities). In the papers of Tippet, Chang and Wilson, this new Green's function lead to the excitation of TEM modes in both waveguides [26, 28].

The TEM cell used in the simulation has a width of $a = 40$ mm and a height of $b = 24$ mm. A cross section of the TEM cell with the important dimensions is shown in Figure 6. The cutoff frequencies of the higher order TE and TM modes can be approximated by the same formula, shown in Equation 41 for rectangular waveguides. However, this is only true, if the septum is very thin ($t/b \ll 0.1$), and for modes with n-even subscripts, i.e. $\text{TE}_{m,2n}$ and $\text{TM}_{m,2n}$ modes.

Maybe calculate with Green's function as in [29]. The resulting radiation resistance might also be helpful later to interpret simulation results.

$$f_c = \frac{c}{2} \sqrt{\left(\frac{m}{a}\right)^2 + \left(\frac{n}{b}\right)^2} \quad (41)$$

- f_c : cutoff frequency of the mode T_{mn}
- c : speed of light in the medium (approximately 3×10^8 m/s in air)

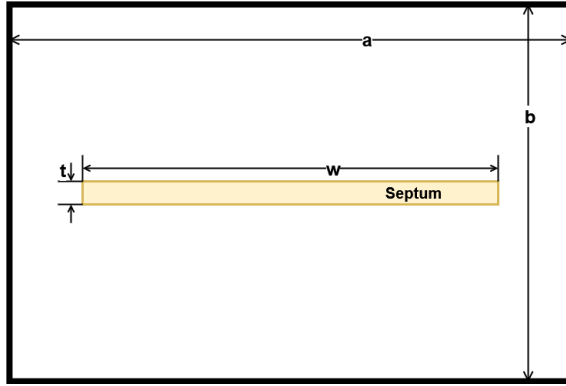


Figure 6: Cross section of the TEM cell

- a : wider dimension (broad wall) of the rectangular waveguide (meters)
- b : narrower dimension (narrow wall) of the rectangular waveguide (meters)
- m : mode index in the a -direction (integer, $m \geq 0$)
- n : mode index in the b -direction (integer, $n \geq 0$)

The cutoff frequency of the TE_{10} mode is around 3.75 GHz, according to Equation 41. To verify this, a modal analysis was performed in Ansys HFSS, where an empty TEM cell was modeled with two waveports defined at its output. The resulting S_{12} -parameters are presented in Figure 7. The black line shows the S_{12} -parameter over the frequency of the TEM mode, while the blue line demonstrates S_{12} -parameter of the TE_{10} mode. At a frequency of 3.75 GHz, the mode propagates without attenuation, where the cutoff frequency $f_{c,10}$ is defined. The simulated result comes very close to the analytically determined one.

The red trace shows a cutoff frequency of $f_{c,10} = 3.12$ GHz for the TE_{01} mode. Equation 41 would predict a cutoff frequency of 6.25 GHz, however, the septum influences n-odd modes like this one. Their cutoff frequencies are shifted to a lower value [27].

The frequency in simulations with the TEM cell will range from 1 MHz to 3 GHz. This guarantees that the higher order modes will not influence the simulation results.

In a real TEM cell, a tapered section transforms the TEM waveguide to a coaxial transmission line. This section does not cause reflections of waves in TEM mode. However, higher order TE and TM modes get reflected, and because the TEM cell is a high-Q cavity, resonances occur at $\frac{\lambda}{4}$ or $\frac{\lambda}{2}$ [12]. This is not considered in these simulations, since the simulation model does not contain this tapered section.

The TEM cell does not only support TEM modes, above their cut-off frequency TE and TM modes begin to propagate. Because the TEM cell is a high-Q cavity, those cut-off frequencies are sharply defined frequencies. Due to imperfections, changes in materials or finite conductivity of the conducting plates, wave propagation in the TEM mode may excite higher order TE and TM modes, too [13]. A change in material, for example, demands the electric and magnetic field to have a component in the direction of propagation at the discontinuity. A paper by Wilson and Ma present analytical approximations to determine

Maybe do simulations with such a tapered section. See [12]

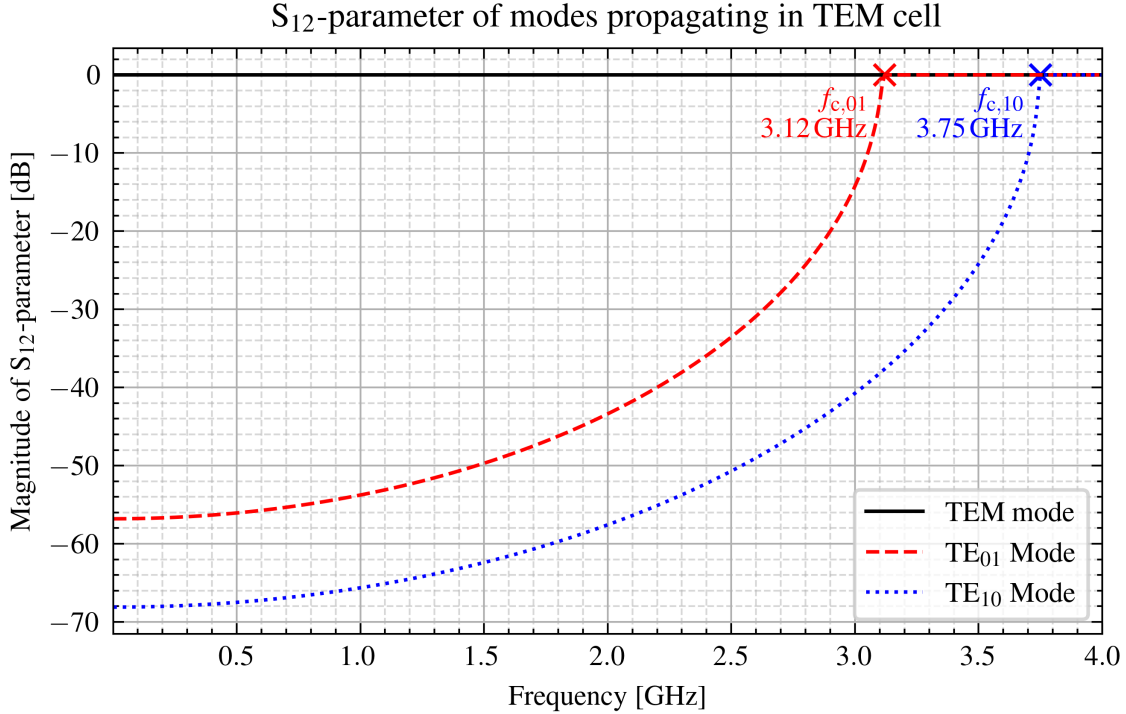


Figure 7: Propagation of TEM, TE₀₁ and TE₁₀ modes in TEM cell

these frequencies [31]. There is a long list for the several first few corner frequencies of the first modes. Additionally, a paper by Koch, Groh and Garbe determines the resonance frequencies of the first TE modes analytically [13]. The TEM mode is necessarily excited by the geometry of the TEM cell, hence this mode is called essential. The higher order TE and TM modes, which are only excited due to non-uniformity of the TEM cell, are called non-essential modes [12].

The first modes propagating after the TEM mode is the TE₁₀ and TE₀₁ modes. Their transversal electric fields are depicted in Figure 8.

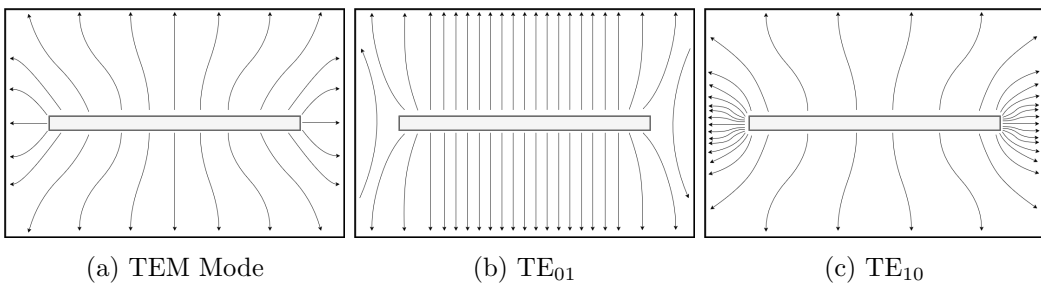


Figure 8: Transversal electric fields in cross section of TEM cell

Vector directions are wrong in the pictures. Additionally, update cutoff frequencies.

2.6 Electrically Small Radiating Sources in TEM Cells

An electrically small radiating source may be represented by six dipoles. This number includes three magnetic dipoles pointing in every direction of the Cartesian coordinate system (x, y, and z-direction), and three electric dipoles in the same orientation. Consequently, an equipment under test (EUT) could be modeled with these dipoles, leading to much less computational effort in simulation. The excited EM waves by point sources is discussed in [6] and in subsection 2.5. An analytical procedure to determine these dipole moments is presented by Sreenivasiah [23], and some experimental results based on it can be found in the research of Kreindl, where bond wires were modeled with magnetic dipoles[15], and, again, Sreenivasiah [23].

The idea is to place the EUT in the TEM cell and measure the power of both output ports. The amplitudes of the TEM fields are expressed by Equation 42 [23].

$$\begin{pmatrix} a \\ b \end{pmatrix} = \frac{1}{2}(-\mathbf{m}_e \cdot \mathbf{E}_0^\pm + i\omega\mu_0\mathbf{m}_m \cdot \mathbf{H}_0^\pm) \quad (42)$$

The magnetic field \mathbf{H}_0 and electric field \mathbf{E}_0 are both normalized to $1\sqrt{\text{Hz}}$ [15] and correspond to the TEM mode in free space [23]. The electric dipole moment \mathbf{m}_e and the magnetic dipole moment \mathbf{m}_m are complex vectors, containing an amplitude and phase for every one of the three directions in the coordinate system (x, y, z), and have the units $\text{A} \cdot \text{m}$ and $\text{V} \cdot \text{m}$. The variables a and b correspond to the amplitudes of the waves in both possible directions in the TEM cell with the unit $\sqrt{\text{W}}$. This leads to the final form in Equation 43 [23].

$$\begin{pmatrix} a \\ b \end{pmatrix} = -\frac{1}{2}(\mathbf{m}_e \pm i\mathbf{k}\mathbf{m}_m \times \mathbf{z}) \cdot \mathbf{e}_0 \quad (43)$$

The unity vector \mathbf{z} points in direction of propagation. The function vector \mathbf{e}_0 describes the normalized electric field amplitude in traverse direction, i.e. x and y-directions, of the excited fundamental mode. Due to the normalization of the electric and magnetic fields to $1\sqrt{\text{W}}$, the total power at one port is 1 W. This defines \mathbf{e}_0 as the electric field when the TEM cell is excited with a peak unit power, since the amplitude of the electric field is considered, not the RMS value.

Note, that an electric dipole in the TEM cell leads to a increase in power with the same phase in both ports, and a magnetic dipole leads to the same increase, but with a phase shift of 180° . This also explains why the EUT shall be place halfway on the septum in x-direction. Any shift from this position changes this phase shift from 180° . It is therefore required to measure the power of the ports with phase information, like using a complex Poynting vector, which is easy to implement in a simulation software. When measuring a device with a real TEM cell, the phase information may be found by summing and subtracting the output powers of the ports, as is shown in [23].

peak power, not average. Explain better.

Additionally, only the electric or magnetic dipole moment, that is aligned with the electric or magnetic field in the TEM cell, influences the output power, ideally. Furthermore, in

the optimal case, the EUT is placed in the dead center of the TEM cell, where the x- and z-component of \mathbf{e}_0 in the $y=0$ plane becomes zero due to symmetry [23]. If this is not the case, the measurements may vary significantly [16].

The formula has originally been derived for cylindrical waveguides [6]. There, the position of the electric and magnetic dipole moments do not matter, as long as the matching electric and magnetic fields at the surfaces are chosen. This is because the field components do not change direction when propagating from the dipoles to the surfaces, due to the symmetrical property of the cylindrical waveguide. This is not the case for a TEM cell. There, an offset into the x- and y-direction from the center leads to field components, which change direction while traveling to the surfaces. Then, the vector product used in the derivation by Lorentz Reciprocity theorem is not valid anymore. Instead, the fields at the test points have to be considered, and because they don't have a singular x,y or z-component anymore, several more dipole moments become relevant.

However, in a TEM cell, the normalized electric field strength is not necessarily symmetrical. Therefore, it must be found out, depending on the position of the dipole moment. In dead center, the normalized electric field only has a z-component. However, with an offset towards z- or y-direction, it will have a y-component, too. Then, the normalized electric field \mathbf{e}_0 can be found with through Equation 44a for and Equation 44b. For these equations, a known electric dipole moment m_{se} is used for both the x- and z-direction. P_x and P_z describe the output powers at one port, depending on the electric dipole's orientation [23]. When knowing the normalized electric field \mathbf{e}_0 at this point, any magnitude of electric dipole moments may be derived by scaling the coefficients a and b . When only considering dipole moments in z-direction, then only Equation 44b is needed.

$$e_{0x} = \frac{2\sqrt{P_x}}{m_{se}} \quad (44a)$$

$$e_{0z} = \frac{2\sqrt{P_z}}{m_{se}} \quad (44b)$$

The normalized electric field of the TEM mode is then given by Equation 45a in x-direction and by Equation 45b in z-direction [31]. The equations follow from the singular integral-equation approach in [28]. The formula is not valid for the gap regions. However, since there isn't any dipole moment to expected there, it should still suffice.

$$e_{ox} = \frac{2}{a} Z_c^{1/2} \sum_{m_0=1}^{\infty} \frac{\sinh M(b-pz)}{\sinh Mb} \cdot \sin Mx \sin Ma J_0(Mg) \quad (45a)$$

$$e_{oz} = p \frac{2}{a} Z_c^{1/2} \sum_{m_0=1}^{\infty} \frac{\cosh M(b-pz)}{\sinh Mb} \cdot \cos Mx \sin Ma J_0(Mg) \quad (45b)$$

Z_c is the characteristic wave impedance, a is half the width of the TEM cell, b is half its height. The sign-function $p = 1$ above the septum, and $p = -1$ below it. $M = m\pi/2a$ and g is the length of the gap between the septum and the conducting wall. The index $m = 1, 3, 5, \dots$ is iterated over odd integers.

The electric field / magnetic field distribution

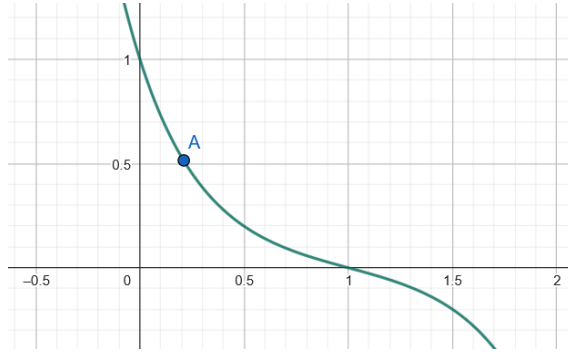


Figure 9: Normalized e-field distribution along z-axis at center of septum

2.7 Shielding

Effective shielding is of great interest to reduce EMI of electronic systems. A figure of merit for shielding capabilities of a material is the electromagnetic shielding effectiveness (SE), given in Equation 46 [7]. E_i is the incident electric field, while E_t is the transmitted electric field, also depicted in Figure 10. It depends on the thickness and shape of the material, and its electric and magnetic properties. Additionally, the TEM cell contributes to the SE values.

$$SE_{dB} = 20 \log \left(\frac{E_i}{E_t} \right) \quad (46)$$

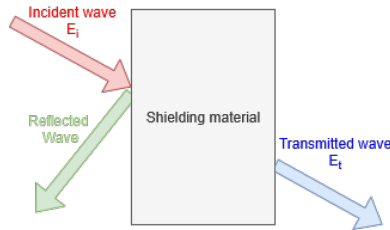


Figure 10: Incident, reflected and transmitted electric fields due to interaction with shielding material

An electromagnetic wave may undergo several reflections inside the shielding material, with each reflection adding up to the total reflected, absorbed and transmitted waves. The total shielding effectiveness is therefore determined by Equation 47, according to Schelkunoff. A_{dB} represents the absorption losses traveling through the shield, R_{dB} the reflection losses, and B_{dB} is the correction factor for the multiple reflections inside the shield [7].

$$SE_{dB} = R_{dB} + A_{dB} + B_{dB} \quad (47)$$

Calculate with S-params S_{11} and S_{21} : A, R and T.

This approach to shielding with internal re-reflections in the shielding material was derived by Schelkunoff. https://www.ieee.li/pdf/viewgraphs/fundamentals_electromagnetic_shield.pdf

The reflections occur due to the change in wave impedance. They are described through a reflection coefficient R . Additionally, it is common to normalize the wave impedance Z to the free-space wave impedance Z_0 . At the interface from free-space to a shielding material, this leads to Equation 48 [6].

$$R = \frac{Z - 1}{Z + 1} \quad (48)$$

$$Z = \frac{1}{Z_0} \sqrt{\frac{i\omega\mu}{\sigma + i\omega\epsilon}} \quad (49)$$

The reflection coefficient can be converted into dB, leading to R_{dB} . Any additional reflection happen due to re-reflections inside the shielding material, described by B_{dB} . The rest of the energy must either be absorbed, described by A_{dB} or transmitted, shown by T_{dB} .

The wave number k in lossy media is described in a real and imaginary parts as in Equation 50. The imaginary part α is the attenuation or absorption coefficient. It describes the reduction of the intensity of the wave, which occurs with $e^{-\alpha x}$, where x is the coordinate direction of propagation. The real part $\beta = \frac{2\pi}{\lambda}$ is the phase constant [11].

$$k = \beta + i\frac{\alpha}{2} \quad (50)$$

$$\mathbf{E} = \mathbf{e} \cdot e^{ikx} \quad (51)$$

When the molecules in a material are exposed to electric fields, they will polarize, described by their permittivity ϵ . When exposed to a magnetic field, the spinning of their electrons in the atoms align with the magnetic field, described by the permeability μ of the material. When the fields alternate over time, the molecules will always move and align according to them. This is essentially a movement of charges, and therefore described by a conductivity σ . The energy lost in this process is dissipated as heat [1].

The electric field will push charges in polarizable molecules apart. This separation of charges may be described as an electric dipole, depending on the separation distance and the charge. Under alternating electric fields, the moving of charges will contribute to σ . This phenomenon is called dielectric hysteresis. Equation 52 quantifies it by a loss tangent $\tan \delta_e$ [1]. There, σ_s is the static conductivity, meaning the conductivity of the material for static fields. The complex part of the permittivity ϵ'' describes the lossy part of the dielectric material, specifically relevant for the alternating fields case. The real part of the permittivity is lossless and is noted by ϵ' . The overall complex permittivity is therefore $\epsilon = \epsilon' + i\epsilon''$.

$$\tan \delta_e = \frac{\sigma_s}{\omega\epsilon'} + \frac{\epsilon''}{\epsilon'} \quad (52)$$

p. 309
Classical
Electrodynamics
(John
David
Jackson)
describe
shielding
material
by dipole
moments

Formula
 α ?
Needed?

S-
parameters
should
enable
derivation
of α . Due
to normal
incident
wave of
TEM,
no angle
needed to
consider.

Basics:
Balanis
2012 page
68?

The loss tangent therefore $\tan \delta_e$ relates the conductivity of a material to the real permittivity. A dielectric with low losses has a much larger displacement current than conduction current density ($\tan \delta_e \ll 1$). The opposite is true for a good conductor ($\tan \delta_e \gg 1$) [1].

The loss tangent $\tan \delta_e$ is a function of frequency, however, it is often not stated as such. Therefore, the loss tangent of FR4, for example, is given as $\tan \delta_e = 0.02$ for frequencies up to 1 GHz. For higher frequencies, the molecules may have resonance frequencies, where they influence more strongly the overall conductance and consequently increase the imaginary part of the permittivity ϵ'' .

There are also magnetically lossy materials, which is introduced by a complex permeability $\mu = \mu' + i\mu''$. Analog to the dielectric case, the permeability can also be described by a loss tangent $\tan \delta_m$ as shown in Equation 53. However, the loss tangent is very low for the majority of materials and will be neglected. Ferrites are an exception, which are commonly used to dampen high frequency signals [1].

$$\tan \delta_m = \frac{\mu''}{\mu'} \quad (53)$$

Electric fields dominate in the near-field region of electric dipoles. To shield them, high permittivity and high conductivity materials, ideally with a high loss tangent $\tan \delta_e$ shall be used. On the other hand, magnetic fields dominate in the near-field region of magnetic dipoles. For shielding them, high permittivity and high conductivity materials, again with a high loss tangent $\tan \delta_m$ shall be used.

describe
 α and δ
for ab-
sorption.
Then re-
flections
with ϵ
and μ
source

2.7.1 ASTM ES7-83 Method

The ASTM ES7-83 method is used to determine the shielding effectiveness of shielding materials. The shielding material is inserted into a coaxial TEM cell around the septum. Ideally, they form a continuous connection [21].

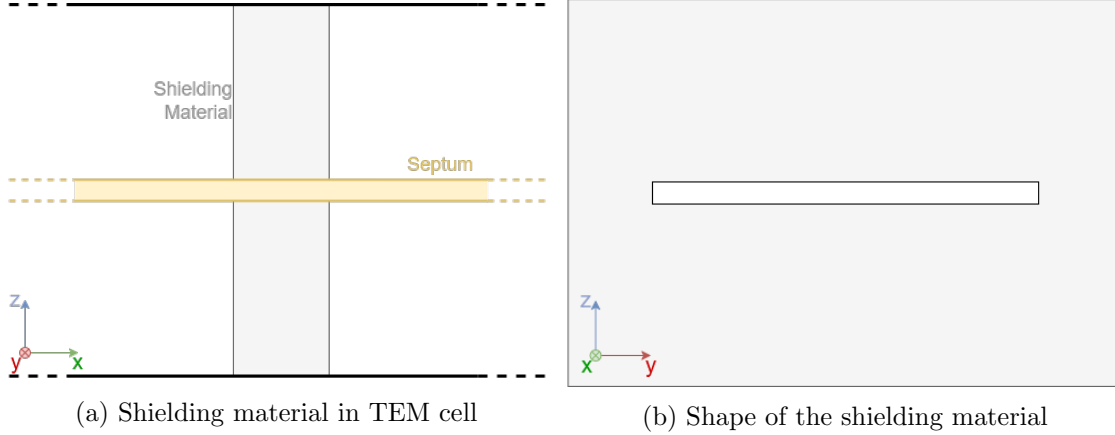
In this method, two measurements are performed with an oscilloscope attached to the output of the TEM cell. In the first, an empty TEM cell is excited and a reference output voltage U_{ref} is measured. In the second, the TEM cell is loaded with the shielding material, and the output voltage U_{load} is again noted. The measurement values are then used in Equation 54 to derive the shielding effectiveness SE_{dB} [21].

$$SE_{\text{dB}} = 20 \cdot \log \left(\frac{U_{\text{ref}}}{U_{\text{load}}} \right) \quad (54)$$

In the case of simulating the problem, such a procedure may be used, too. It is more convenient, then, to defined a reference output power P_{ref} for an unloaded TEM cell, and a output power for the loaded case P_{load} . This leads to the similar Equation 55.

$$SE_{\text{dB}} = 10 \cdot \log \left(\frac{P_{\text{ref}}}{P_{\text{load}}} \right) \quad (55)$$

Additionally, a rectangular TEM cell is used for this method, instead of the commonly used cylindrical version. Figure 11b shows the cross section of this shielding material, which is inserted into the TEM cell. In Figure 11a the shielding material can be seen wrapped around the septum.



Then, the S-parameters derived in the simulations are used to get to the output powers P_{ref} and P_{load} . By exciting the TEM cell with a power of 1 W, the reference power $P_{\text{ref}} = 1 \text{ W}$. The measured power is then derived through Equation 56.

$$P_{\text{load}} = P_{\text{ref}} \cdot 10^{|S_{12}|/10} \quad (56)$$

2.7.2 Dual TEM cell

The shielding effectiveness of a material may also be determined using two TEM cells, which are stacked upon each other, as shown in Figure 12. They are connected through an aperture, which can be filled with the shielding material. One TEM cell is excited, and therefore acts as a driving cell. It transmits power through the aperture. It is measured at the second TEM cell, which acts as a receiver. The dual TEM cell simulates near-field conditions, opposed to the far-field conditions simulated by the simple TEM cell [21]. This is important when using the shielding material to shield an antenna's radiation by placing the material directly next to it.

The electrically small aperture may be described by an electric and a magnetic dipole moment. Their magnitude is related to the electric and magnetic coupling between the TEM cells over the aperture. Therefore, the electric and magnetic coupling can be determined separately by adding or subtracting the output powers of the receiving TEM cell [21, 30]. Consequently, an electric shielding effectiveness SE_{dB}^e can be calculated with Equation 57a, and a magnetic shielding effectiveness SE_{dB}^m with Equation 57b. If a material, for example, permits energy transfer because of magnetic dipoles in it, then a measurement with lower SE_{dB}^m than SE_{dB}^e is to be expected [30].

Describe Method.
Then follows dual TEM cells

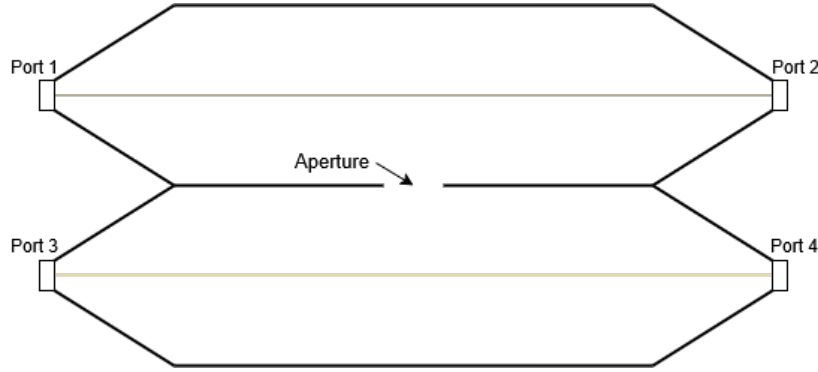
must it be electrically small?

$$SE_{\text{dB}}^e = 10 \log \left(\frac{P_{\text{ref,sum}}}{P_{\text{load,sum}}} \right) \quad (57a)$$

$$SE_{\text{dB}}^{\text{m}} = 10 \log \left(\frac{P_{\text{ref,diff}}}{P_{\text{load,diff}}} \right) \quad (57\text{b})$$

Because the normalized electric field at the aperture will be of TEM mode, only the component normal to the aperture in z-direction has to be considered. Just as in the case of dipole representation, the Lorentz Reciprocity theorem may be applied to find the fields in the TEM cell. Because both the fields at the output and in the aperture are of TEM mode, only the E-field at the output may be considered.

Since the aperture is electrically small, the field quantities may be assumed to be constant over it. This makes it possible to represent the energy transfer by dipole moments.



Polarization
of the
material.
Small
aperture
theory.

Figure 12: Dual TEM cell with aperture

3 Antennas

3.1 Antennas to Investigate

3.1.1 IFA

3.1.2 Center fed monopole antenna

3.2 Crossed dipole antenna

A crossed dipole antenna radiates very evenly into every direction. This could be interesting to use, in order to excite several modes, especially in the presence of shielding materials.

When this antenna is near a perfect electric conductor (PEC), the gain becomes dependent on the distance to it. At a distance of $H = 0.25\lambda$, the gain reaches a maximum due to constructive interference in normal direction to the PEC surface. When the distance is small, the image currents may cancel and the gain decreases. Therefore, the output power on the TEM cells depends on the distance, and implicitly on the frequency. This means that the frequency behavior of the representing dipoles may vary from a standard dipole.

Additionally, when a shielding material is present, different modes may be excited, which also influence the behavior. Those different modes depend on all 6 dipole moments, with which the antenna shall be modeled.

4 Simulations

4.1 Antennas

4.1.1 Inverted F-antenna

The inverted F-antenna (IFA) is modeled in Ansys HFSS as shown in Figure 13. Its material is copper. It is positioned at the center of the TEM cell, mounted at the top surface. The 5 mm long wire points towards waveport 2. The excitation is a modal wave port. With a maximum dimension of 5 mm, the antenna is electrically small for a frequency of up to 6 GHz, at which it will be a tenth of the wavelength. In this simulation, the antenna is investigated for the frequency of 100 MHz to 1 GHz. The TEM cell has a width of 40 mm and a height of 24 mm and an impedance of $\sim 50 \Omega$. The goal is to find equivalent dipole moments of the antenna.

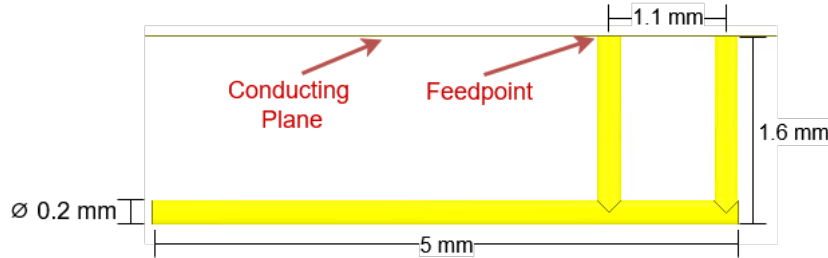


Figure 13: Inverted F-antenna used in the simulation

The coupling between the antenna and the two ports of the TEM cell are described by S-parameters, specifically the forward transmission coefficients S_{A1} and S_{A2} . Figure 14 shows the magnitude of this coefficient, which is the same for the antenna to both ports ($|S_{A1}| = |S_{A2}|$).

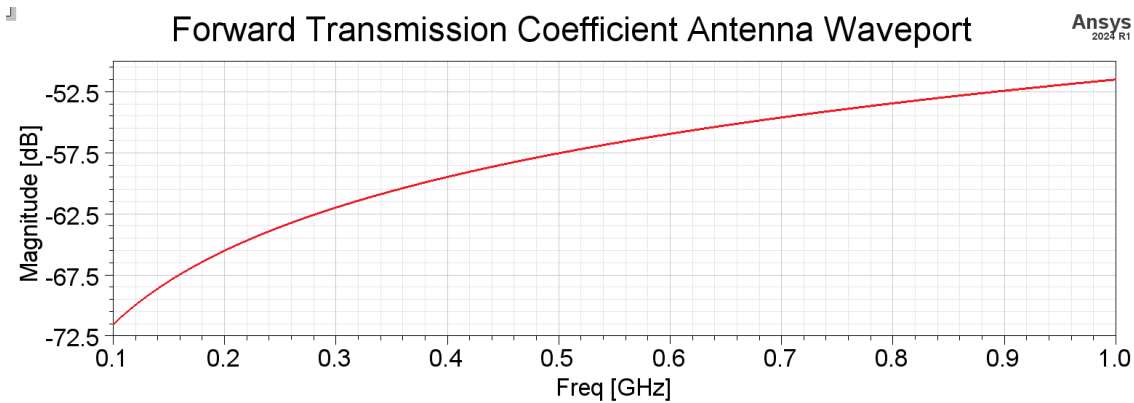


Figure 14: S-parameter describing coupling of antenna to waveport 1

$$P_{\text{Antenna}} = \frac{P_{\text{Out1}}}{10^{|S_{A1}|/10}} = \frac{P_{\text{Out2}}}{10^{|S_{A2}|/10}} \quad (58)$$

Equation 58 describes the relation between the input power at the antenna and the mea-

sured output power of the TEM cell. It is defined by the magnitude of the forward transmission coefficients.

$$\iint_A \mathbf{e}_0 \times \mathbf{h}_0 \cdot d\mathbf{A} = 1 \quad (59)$$

Equation 59 shows that the electric field \mathbf{e}_0 and magnetic field \mathbf{h}_0 are normalized to $1/\sqrt{W}$. The surface area A , over which the fields are integrated, is that of the output ports of the TEM cell. The field can be linearly scaled by the complex coefficients a and b , which has been described in Equation 29 and Equation 30. Only one pair of such coefficients is needed, since only the TEM mode is considered.

The coefficients a and b have the unit \sqrt{W} . The fields \mathbf{e}_0 and \mathbf{h}_0 are not known over the whole area. However, the electric field \mathbf{e}_0 has only to be known at one specific point in order to determine the equivalent dipole moments, as will be shown here. The normalization condition therefore leads to an output power equal to $|a|^2/2$ or $|b|^2/2$, respectively, which was also found in [30].

$$P_{\text{out}1} = \iint_A \langle \mathbf{S} \rangle \cdot d\mathbf{A} = \iint_A \frac{1}{2} \Re\{(a \cdot \mathbf{e}_0) \times (a \cdot \mathbf{h}_0^*)\} \cdot d\mathbf{A} = \frac{|a|^2}{2} \quad (60a)$$

$$P_{\text{out}2} = \iint_A \langle \mathbf{S} \rangle \cdot d\mathbf{A} = \iint_A \frac{1}{2} \Re\{(b \cdot \mathbf{e}_0) \times (b \cdot \mathbf{h}_0^*)\} \cdot d\mathbf{A} = \frac{|b|^2}{2} \quad (60b)$$

The phase shifts of S_{A1} and S_{A2} differ, which is shown in Figure 15. The difference of these phase shifts influences the quantity of magnetic dipole moment and electric dipole moments. A large phase shift indicated a large magnetic dipole moments compared to the electric dipole moment, and vice versa. The large difference in phase shifts in Figure 15 lets one expect the first case. However, the phase shift does not influence the overall output power. It is incorporated into the coefficients a and b , by multiplying the term $e^{i\varphi_a}$ or $e^{i\varphi_b}$ to their magnitude. The phase shift of each port is then implemented by φ_a at the port of the coefficient a , and by φ_b at the port of the coefficient b .

The Poynting vector is periodic from $-\pi/2$ to $\pi/2$, hence any phase difference above that value must be corrected by adding π to it.

The output power of each port is then derived through Equation 60a and Equation 60b. So if $|a| = |b| = 1$, then the electric field \mathbf{e}_0 may be measured, when the output power at one port is $\frac{1}{2} W$. Because it is assumed that the TEM cell contains only waves in the TEM mode, the normalization of the electric and magnetic fields can be used to simplify the calculations.

$$\mathbf{e}_0 \times \mathbf{h}_0 = \Re\{\mathbf{e}_0 \times \mathbf{h}_0^*\} \quad \text{for TEM mode} \quad (61)$$

By using Equation 33 and Equation 32, the equivalent dipole moments are derived. Because of Lorentz reciprocity theorem, only fields aligned with the dipole moments get to the output ports. Since only the TEM mode propagates, only the electric dipole moment

Problem with large TEM cell: Formula does not work for large frequencies. The

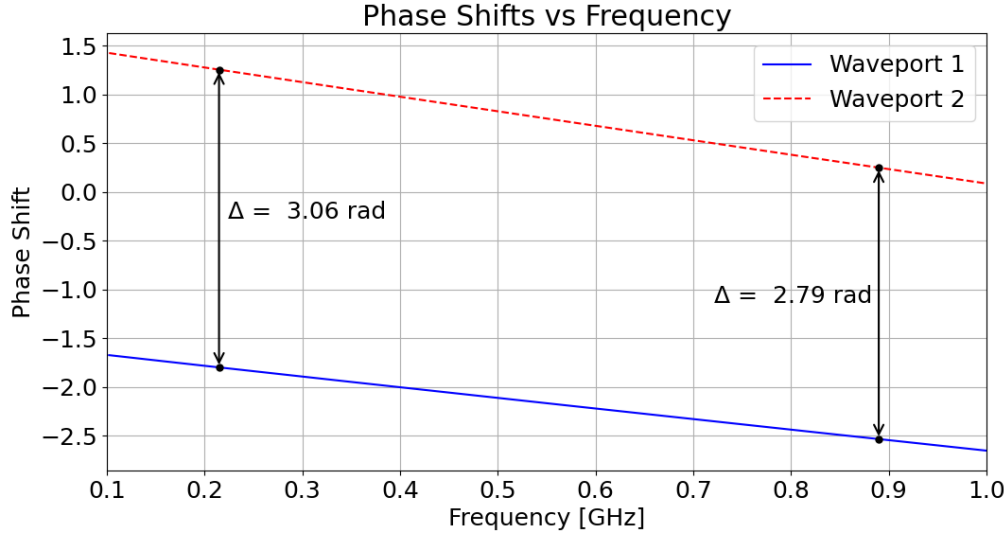


Figure 15: Phase of S-parameters from antenna to waveport 1 and 2

in z-direction and the magnetic dipole moment in y-direction influence the fields. If higher order modes can propagate, the other dipole moments become relevant, too.

$$m_e = \frac{a + b}{e_{0,z}} \quad (62)$$

$$m_m = i \frac{a - b}{k_0 e_{0,z}} \quad (63)$$

Einheitliches
Koordinaten-
system
definieren

By adding or subtracting the coefficients a and b , the dipole moments are expressed into the handy Equation 62 and Equation 63. There, $k_0 = \frac{2\pi}{\lambda}$ is the free space wave number and $e_{0,z}$ is the normed electric field in z-direction at middle height between septum and the upper wall of the TEM cell. However, the height of the measurement point is not important, as the electric field is uniformly distributed along the z-axis. Additionally, the x- and y-components of the electric field \mathbf{e}_0 are zero, which leads to these equations. The dipole moments m_e and m_m are defined to be in the center of the TEM cell, at middle height. If they are shifted in any direction, their approximation would not hold true anymore.

Figure 16 shows the measurement point of $e_{0,z}$. This wouldn't work if the magnetic and electric dipole wasn't defined to be exactly at a height of $b/4$, at dead center. The Lorentz Reciprocity theorem used to derive the formulas take the cross product of the electric field traveling to one output port with the magnetic field caused by the dipole, minus the magnetic field traveling to the same output port minus the electric field caused by the dipole. Since the dipoles are in dead center, the electric field caused by the dipole does only have a z-component, and the magnetic field caused by the dipole only a y-component. If this was not the case, the other components would have to be taken into account of the

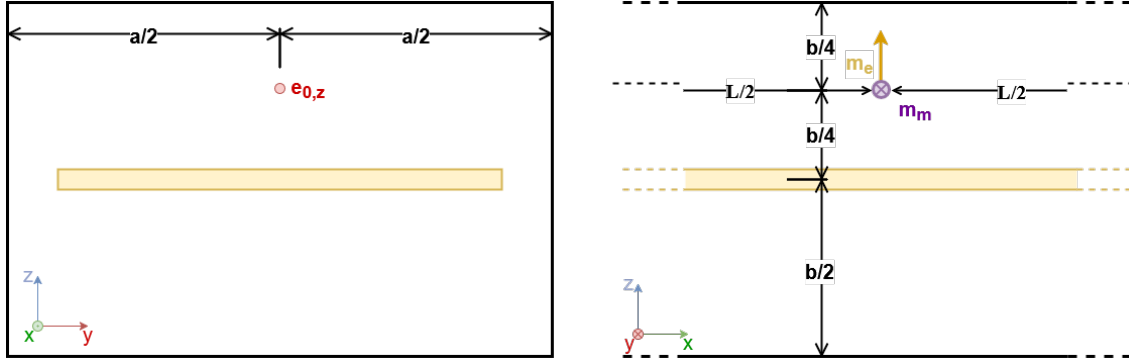


Figure 16: Dipole moments and measurement point of $e_{0,z}$ in TEM cell

fields at the test point. They would already have disappeared at the output ports due to the long travel, and the Lorentz Reciprocity theorem becomes more cumbersome to use. By placing the dipoles in dead center, it is possible to measure the electric field at the output port and normalize it to $\frac{1}{2} \text{ W}$.

Using Equation 11 the magnetic dipole moment can be expressed as a magnetic current. The resulting $m_{m,\text{mag}}$ is shown in Equation 64. The phase shift between the magnetic and electric dipole moments m_{ez} and $m_{my,\text{mag}}$ is always $\frac{\pi}{2}$, which generates the desired TEM wave pattern.

Write clearer.
And put into theoretical part.

$$m_{m,\text{mag}} = im_m\omega\mu_0 \quad (64)$$

The antenna may then be replaced with those two dipole excitations in the center of the upper half of the TEM cell. The magnitude and phase of the fields, as well as the output powers, should remain the same as in the case with the antenna. The phase shift may be determined by measuring the phase shifts of the electric fields at both output ports. When applying this described method in a measurement with a real TEM cell, the phase shift may be found by adding and subtracting the output powers of both ports, as is shown in [23].

Is this
CFM or
IFA simu-
lation?

Figure 17 shows the dipole moments over frequency. The electric dipole moment m_e has been normalized to the free-space wave impedance of 377Ω to make the dipole moments comparable. The antenna input power has been set to 142588.47 W , because this leads to an output power of 1 W at a frequency of 1 GHz . The magnetic dipole moment is much larger than the electric dipole moment, because the current loop of the antenna is aligned with the TEM cell's magnetic fields, but the line current is not with the TEM electric fields. The magnetic dipole moments rises linearly with the frequency, which is equal to a quadratic increase of power. Only the TEM modes has been considered in the simulation, as other modes disturb the calculations.

The electric field \mathbf{e}_0 is approximated with Equation 65 for the purpose of interpolation over frequencies and analytical analysis. The constant u is a scaling factor, which must be adjusted to fit the real electric field values. In this case, this constant equals $u = 820.34$.

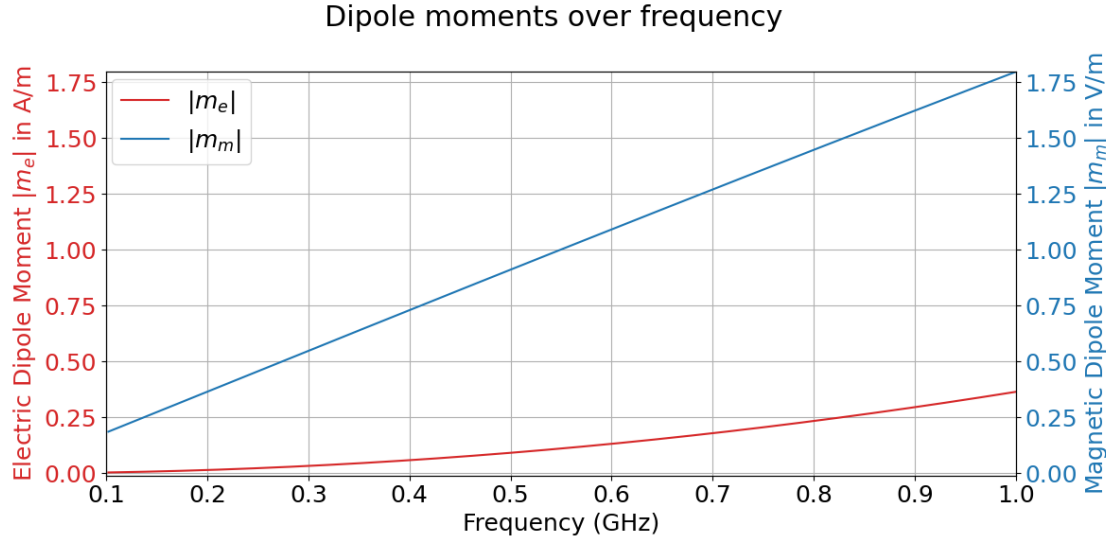


Figure 17: Dipole moments over frequency

The left-hand side term $|a| \cdot e_{0,z}$ is the overall electric field at the measurement point according to Equation 29. Figure 18 shows the resulting plot.

$$|a| \cdot e_{0,z} = \sqrt{2P_{\text{Out}}} \cdot e_{0,z} = u \sqrt{P_{\text{Out}}} \frac{\text{V}}{\text{m} \cdot \sqrt{\text{W}}} \quad (65)$$

The electric field can also be approximated by Equation 66, where $b/2 = 12 \text{ mm}$ is half the height and $Z_W \approx 50 \Omega$ is the impedance of the TEM cell. This works for TEM cells with thin septum. The constant u can be adjusted to fit this equation. The term $\sqrt{2}$ is needed to convert the effective value of the electric field into its magnitude.

$$|a| \cdot e_{0,z} = \frac{\sqrt{2 \cdot P_{\text{Out}} \cdot Z_W}}{b/2} \quad (66)$$

The magnetic coupling with the septum happens due to the alignment of the current loop with the magnetic field of the dominant TEM mode. The antenna is now rotated by 90° around the z-axis, such that the magnetic current loop stands perpendicular to the magnetic TEM fields. Figure 19 demonstrates the phase of the S-parameters, describing the coupling of antenna to waveport 1 and 2. Since the magnetic dipole moment is responsible for a phase between the ports, Figure 19 strongly hints to an absence of it.

?? shows that the electric dipole moment m_e has stayed the same, while the magnetic dipole moment became zero. Consequently, the overall power transfer between the antenna and the waveports is also much lower.

Repeat for different orientations?
Change variable name:
TEM cell height.

The same procedure was repeated with different dipole moments positions,

Electric field approximation and Output Power over frequency

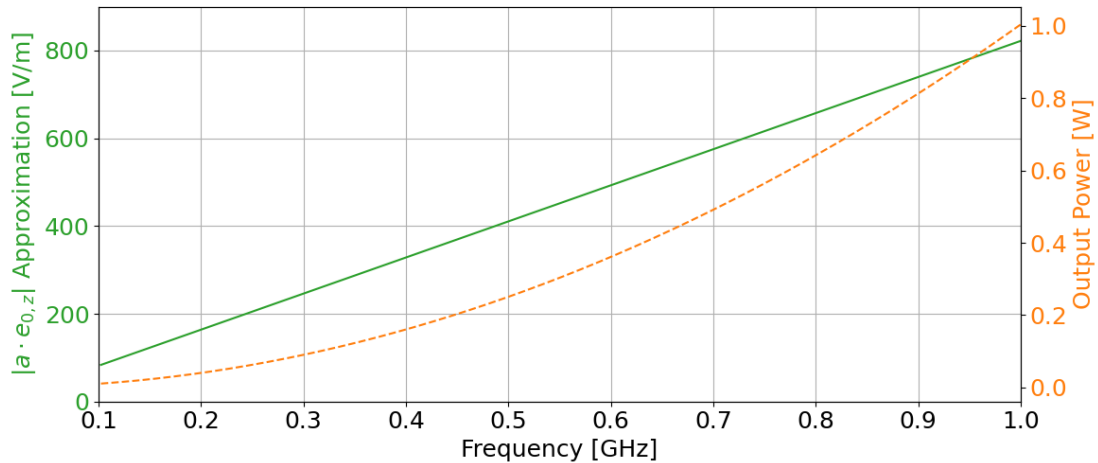


Figure 18: Output power and electric field over frequency

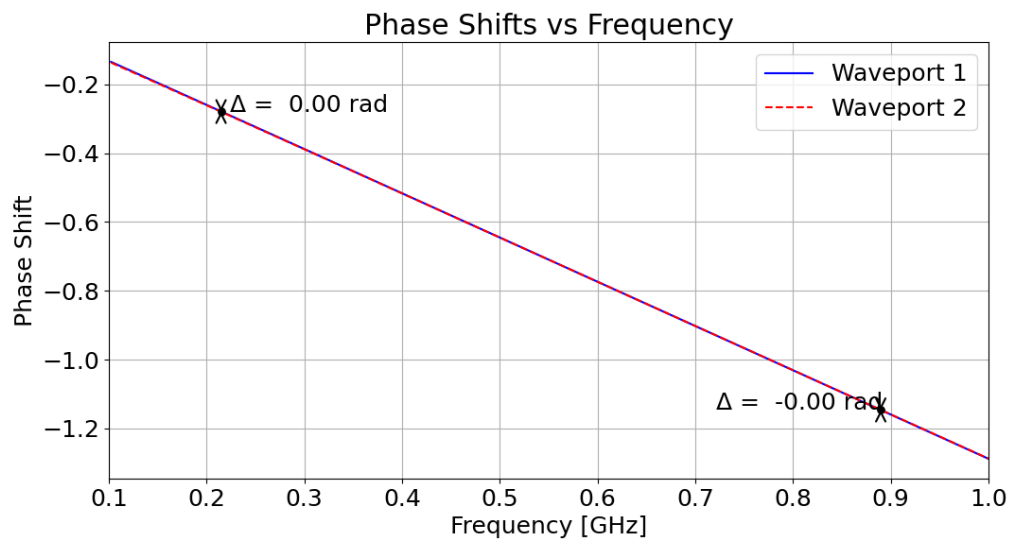


Figure 19: Phase of S-parameters from rotated antenna to waveport 1 and 2

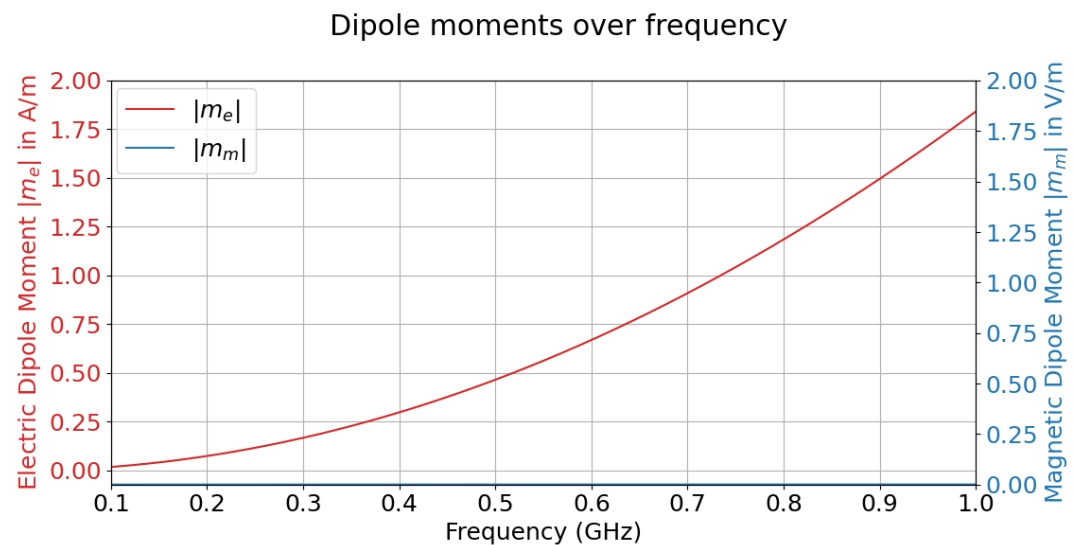


Figure 20: Dipole moments of rotated antenna

4.1.2 Center Fed Monopole Antenna

The center fed monopole antenna is shown in Figure 21. The conducting plane in Figure 21 is on the top side of the TEM cell, thus the image is rotated counter-clockwise by 90 degrees. The electric wire with the length of 5 mm points towards the septum. The 1.1×1.6 mm loop is again aligned with the magnetic field lines of the TEM mode. The antenna is fed with a power of $P_{\text{Antenna}} = 127770.39$ W, which once more leads to an output power of $P_{\text{Out}} = 1$ W at 1 GHz at both output ports.

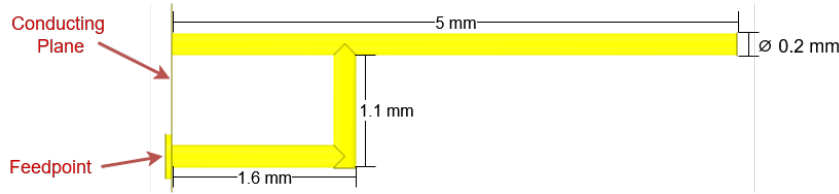


Figure 21: Center fed monopole antenna used in simulation

The magnitude of $|S_{A1}| = |S_{A2}|$ in Figure 22 shows stronger coupling. As will be seen below, this is because of an increased electric dipole moment, while the magnetic dipole moment remained the same. Therefore, the center fed monopole antenna couples well electrically with the TEM cell.

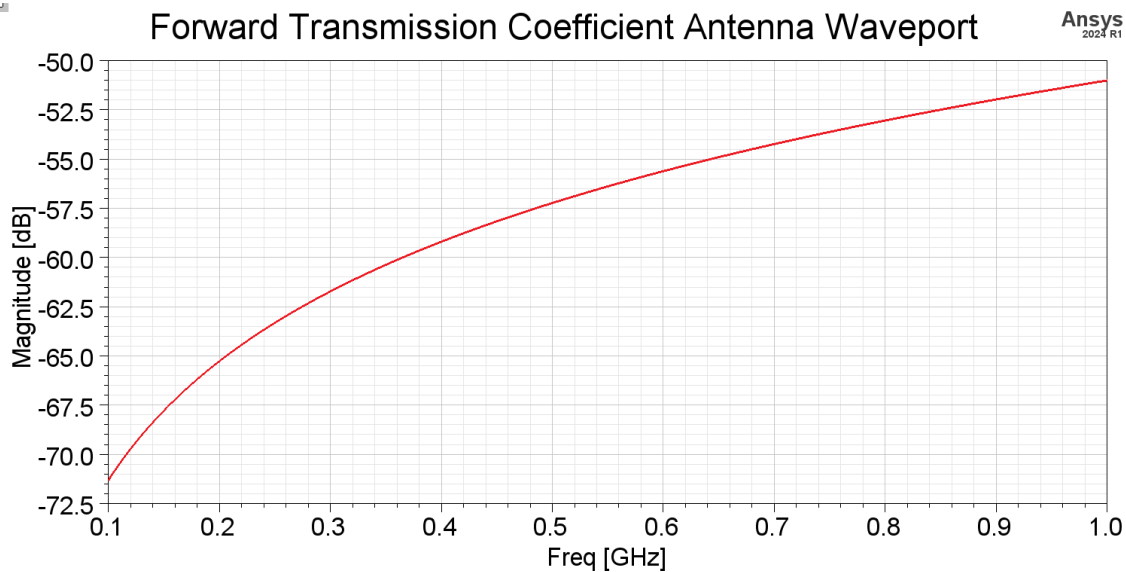


Figure 22: S-parameter describing coupling of antenna to waveport 1

The phase shift in Figure 23 is smaller than in the simulation with the inverted F antenna. This hints to a more influential electric dipole moment than before. This is because of the term $a + b\dots$. When using superposition of each dipole moment...

$$c_1 = \sqrt{a^2 + b^2 + 2ab \cos [(\varphi_a + \varphi_b)/2]} \quad (67a)$$

$$c_2 = \sqrt{a^2 + b^2 - 2ab \sin [(\varphi_a - \varphi_b)/2]} \quad (67b)$$

$$c_1^2 + c_2^2 = a^2 + b^2 \quad (67c)$$

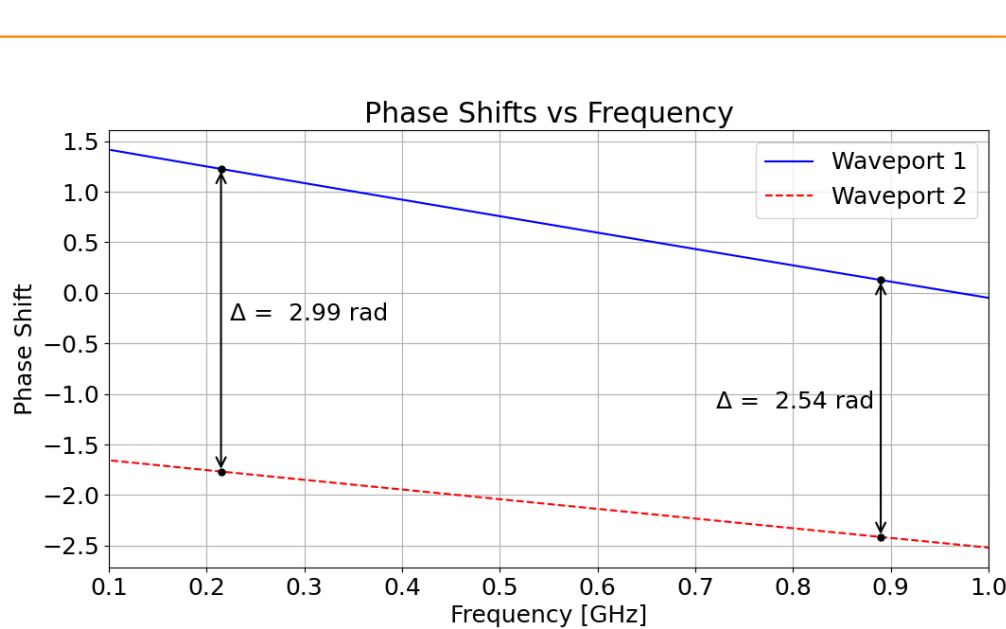


Figure 23: Phase of S-parameters from antenna to waveport 1 and 2

Figure 24 shows that the magnetic dipole moments of the inverted F and center fed monopole antennas are equal. This is due to the same size of the current loops. However, the electric dipole moments increased for the center fed monopole antenna. The alignment of the line current with the TEM cell's electric field causes this. (antenna power = 126549.7191667088 W)

The output power has been scaled as in the simulation before. This leads to the same electric field magnitude. Therefore, the electric field and output power over frequency plot are the same as in the case for the inverted F antenna, visible in Figure 18.

When rotating this antenna by 79°, the electric and magnetic dipole moment influence the output power by roughly the same amount, as visible in Figure 25. This makes itself manifest by a phase shift of around 45° between the output powers of the waveports. Interestingly, both the electric and the magnetic dipole moment demonstrate a non-linear behavior.

not done yet, make it correct

Why does the magnetic moment sink?

CFM at 90° rotation still demonstrates magnetic dipole moment, opposed to cur-

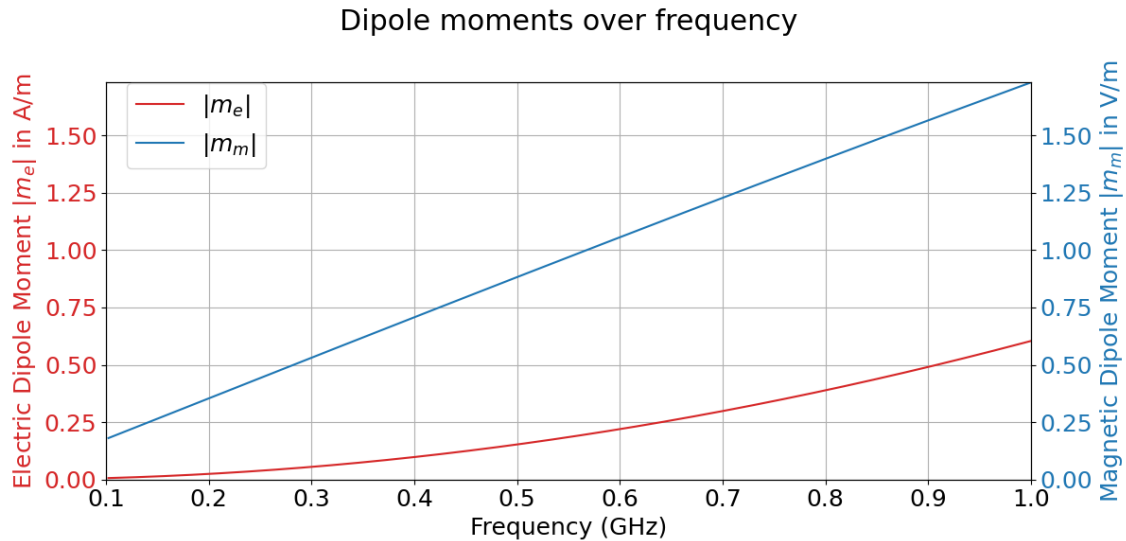


Figure 24: Dipole moments over frequency

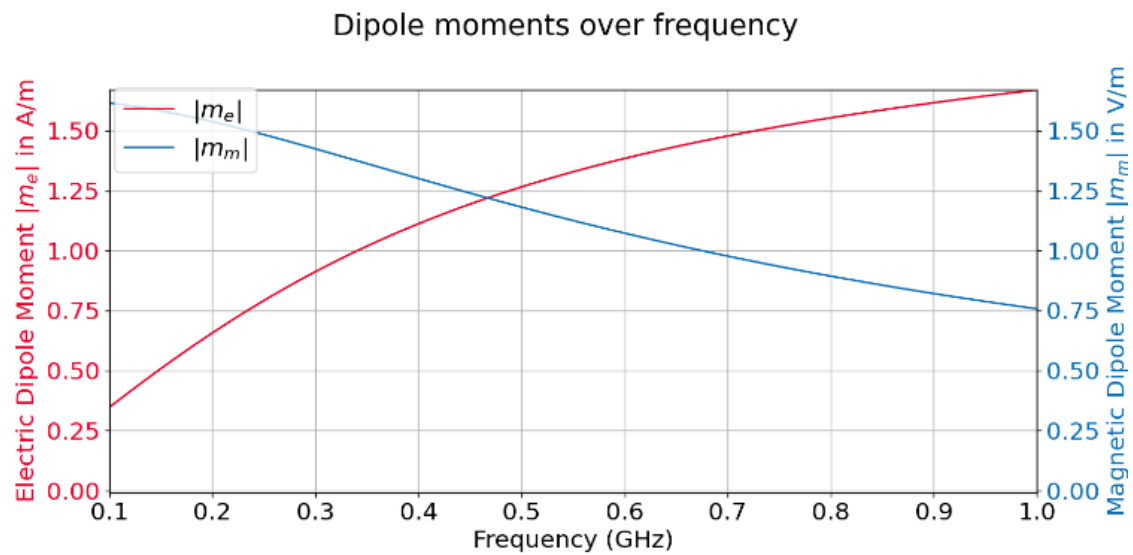


Figure 25: Dipole moments of CFM antenna rotated by 79°

4.1.3 Monopole Antenna

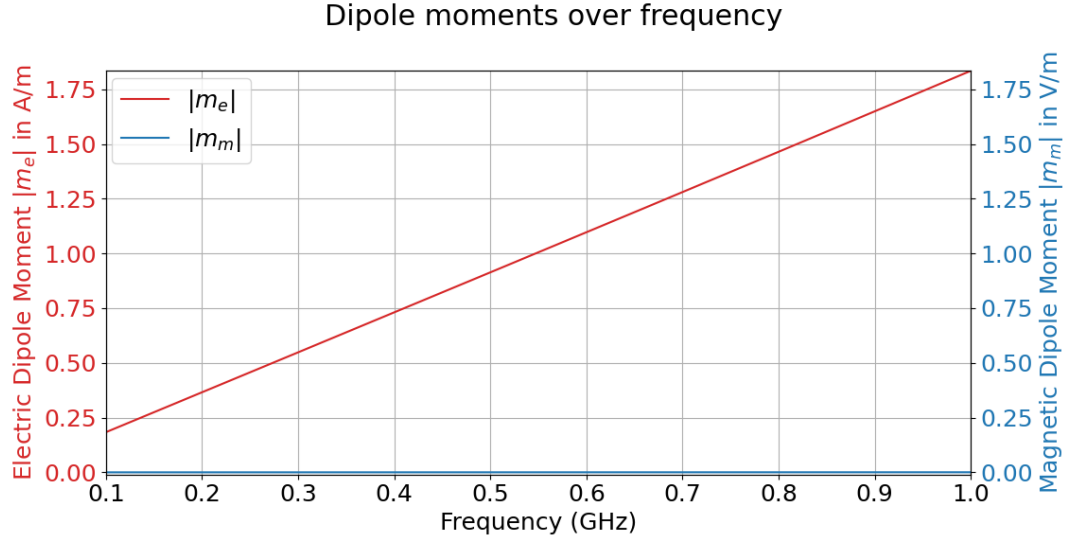


Figure 26: Dipole moments of the monopole antenna

Figure 26 shows the dipole moments of the monopole antenna. Note the linear relation of the electric dipole moment m_e to the frequency, which is not given in the center fed monopole and inverted-F antenna. The magnetic dipole moment equals zero, as expected, due to very weak coupling of the magnetic fields. The length of the monopole antenna is 5 mm.

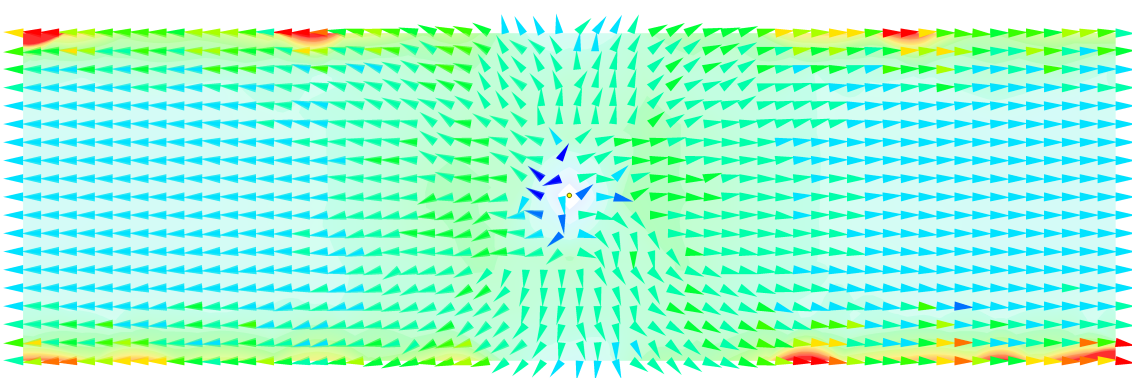


Figure 27: Current surface density at 550 MHz

?? shows the induced surface currents on the septum, when giving the monopole antenna an offset of 7.5 mm. The energy transfer decreases (-1 dB).

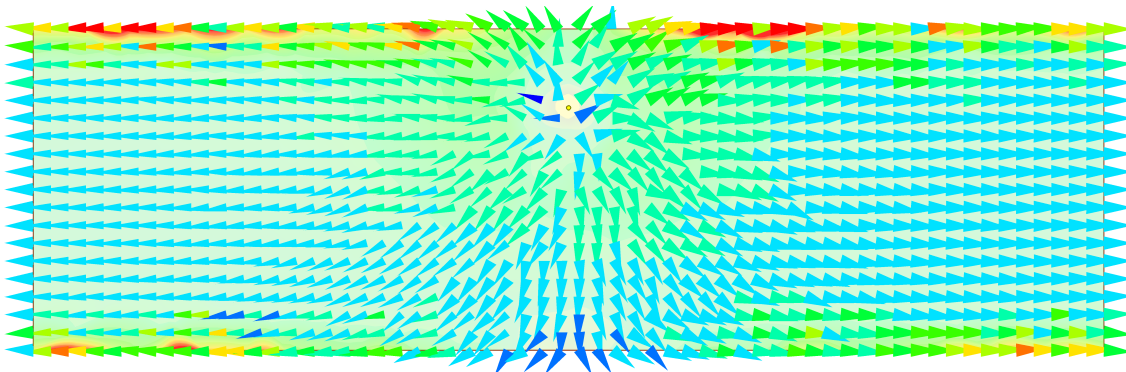


Figure 28: Current surface density at 550 MHz with offset

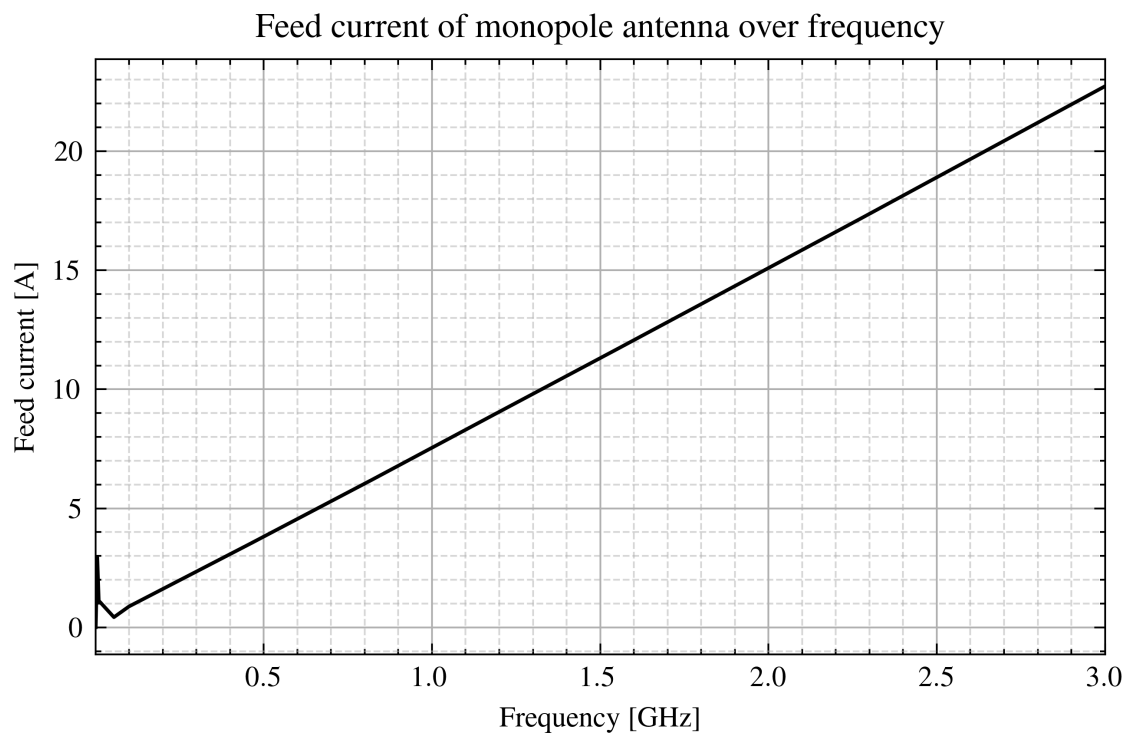
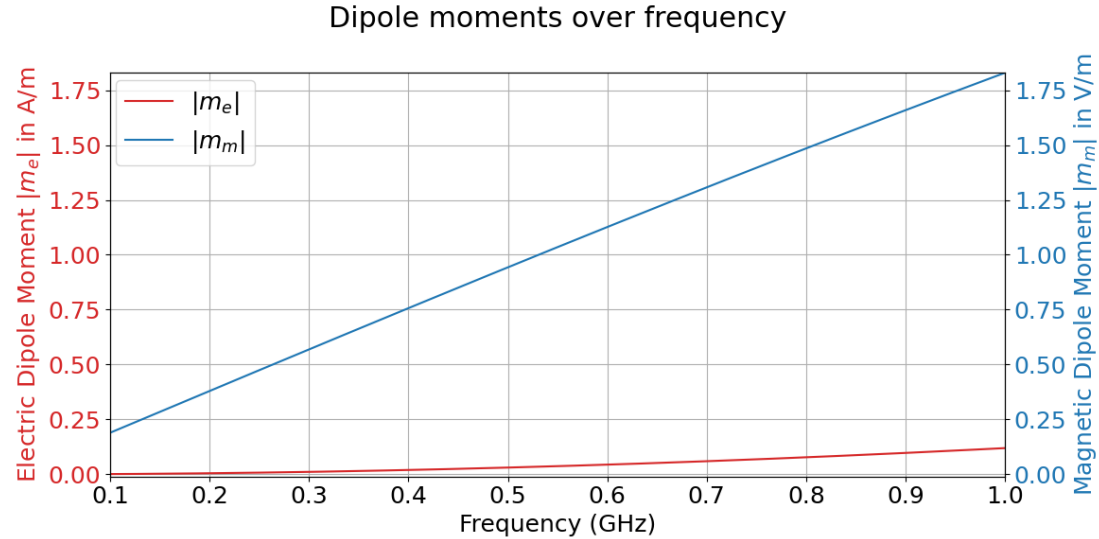


Figure 29: Feed current over frequency of monopole antenna

4.1.4 Loop antenna

A loop antenna of dimensions in form of a square is constructed, with each size having a length of 1.6 mm. This is preferable to a really round antenna, because the adaptive meshing models it much more accurate. The antenna is oriented such that the highest amount of magnetic fields enters it.



Maybe describe this in the HFSS theory part?
Modeling of round surfaces.

Figure 30: Dipole moments of loop antenna

Figure 30 shows the dipole moments of the loop antenna over frequency. As expected, the magnetic dipole moment m contributed the largest amount to the antenna coupling. A small amount of electric dipole moment is also present, which naturally occurs due to the current wire aligned with the TEM electric fields. The electric dipole moment m_e increases non-linearly with frequency.

why?

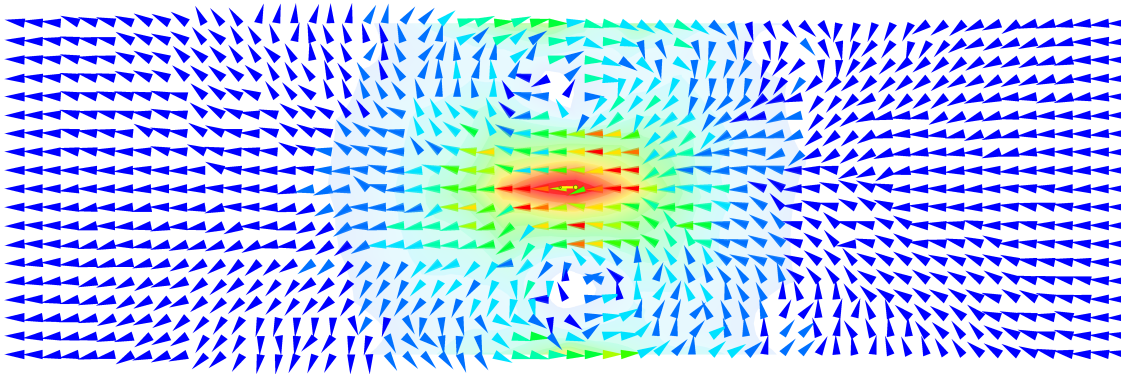


Figure 31: Surface current density at 550 MHz

Note that the surface current density in Figure 31 is much more concentrated in the center. In the case of the monopole antenna, the current density distributed almost equally around the septum. In the case of the loop antenna, the current below the antenna seems to be

cut off by the rotational eddy currents next to them. Furthermore, the phase shift between the currents at the output ports is 180° , leading to the perceived phase shift of magnetic dipole moments.

Figure 32 demonstrates the surface current density when shifting the loop antenna 7.5 cm (quarter of the septum width) in y-direction. The coupling and transferred energy remains roughly the same.

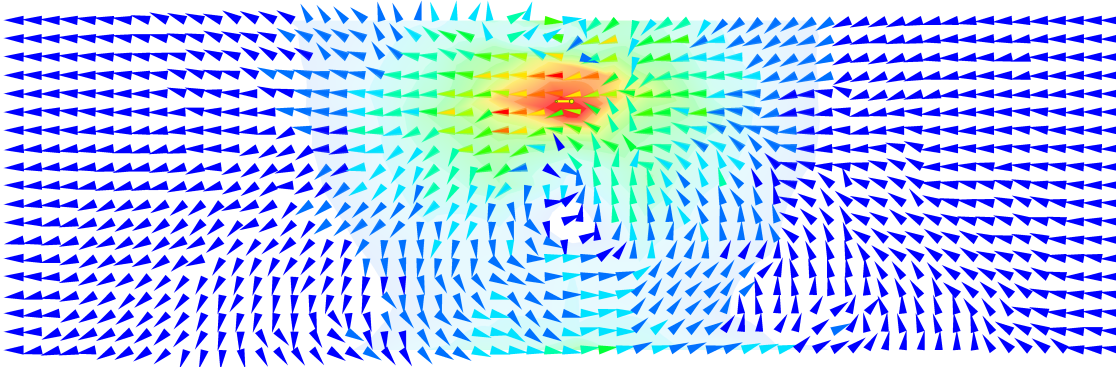


Figure 32: Surface current density at 550 MHz with offset

Find reasons for the eddy current to exist. Maybe there is a nice formula that describes this by maxwell?

Figure 33 shows the surface current density when rotating the antenna by 90° . Only a negligible amount reaches the output ports, leading to no coupling.

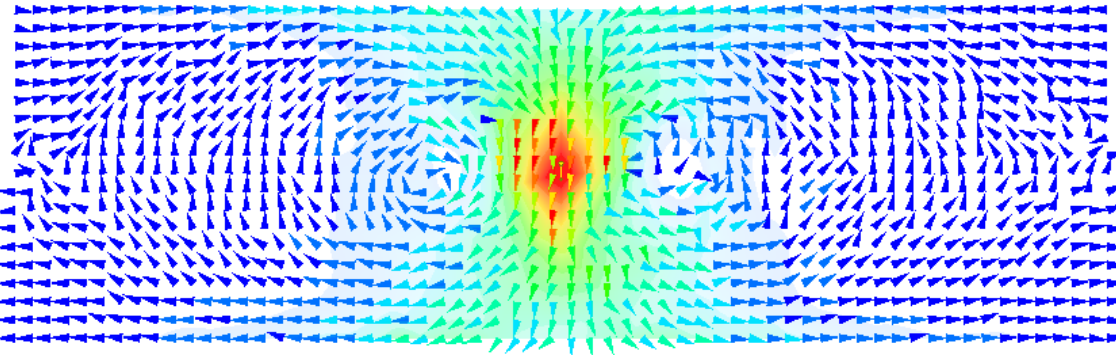


Figure 33: Surface current density at 550 MHz with rotated antenna

Figure 34 shows the current distribution of the current loop antenna, when it is rotated and contains an offset. Again, the eddy currents dominate. However, some of those currents propagate towards the output ports, increasing the energy transfer minimally (0.5 dB). Additionally, the energy transferred is in phase, which makes it indistinguishable from an electric dipole.

Figure 35 shows the charge density distribution in the current loop antenna. Charges collect, among other locations, at the bottom wire. This leads to electric coupling with the septum.

The current and voltage drops along the wire are not constant. From the feedpoint to the first corner, there is a much larger voltage drop and current, than from the second corner

annotate maximum and minimum current densities

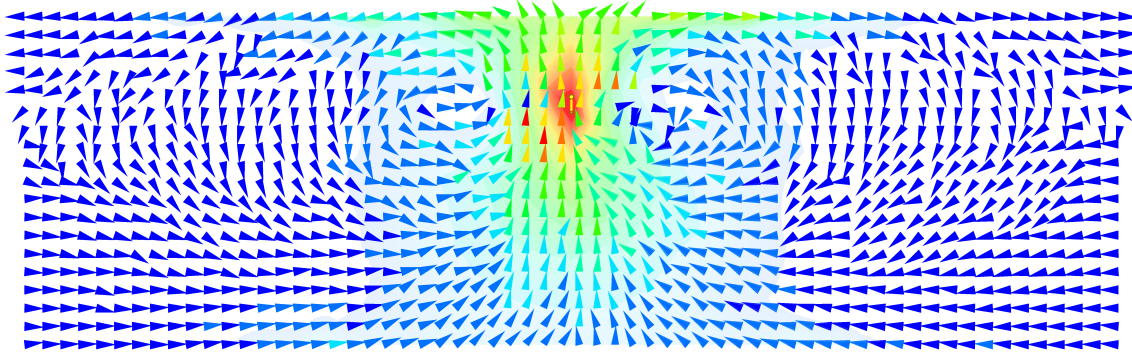


Figure 34: Surface current density at 550 MHz with offset and rotated antenna

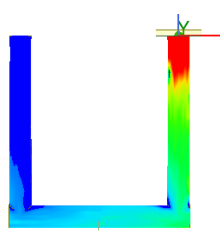


Figure 35: Charge density distribution in current loop antenna

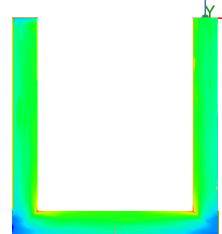


Figure 36: Current density distribution in current loop antenna

to the ground plane. Consequently, the power consumed by the first part is much higher than by the latter. Additionally, this difference in power consumption increases slightly over frequency.

The electric current reduces over the wire because of the displacement current to the septum and the ground plane. As visible in the charge density plot in Figure 36 and the electric field plot in Figure 37, much of the displacement current occurs near the feedpoint and at the wire parallel to the septum. Consequently, this is where the current drops by the most amount.

Insert power consumption plots of each antenna section

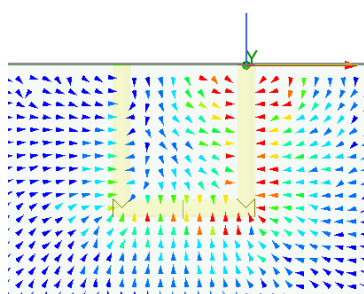


Figure 37: Electric near field in current loop antenna

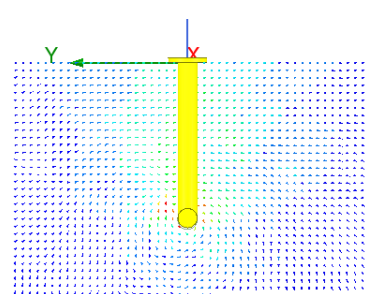


Figure 38: Magnetic near field in current loop antenna

Insert current distribution plots

Figure 40 and Figure 39 show the current and voltage consumption of the antenna. The

H-field from other perspective?

phase shift equals $\phi \approx 89.80$, which hints to a strong inductive behavior. An equivalent circuit is therefore derived in ??, ignoring potential capacitive effects. The inductance is determined to be $L \approx 2.15 \text{ nH}$.

Figure 41 shows the power consumption of the antenna, which is influenced by two factors. The radiation resistance rises quadratically with the frequency. At the same time, the impedance increases, leading to higher matching and therefore to a higher power transfer. This is contrary to the monopole antenna, where the impedance is decreases over the frequency, again leading to better impedance matching, because the impedance was high to begin with. The source impedance is 50Ω .

Figure 42 shows the total power maintained in the system, meaning $S_{11}^2 + S_{12}^2 + S_{13}^2$. It does not add up to one, meaning that some energy is lost due to finite conductivity of the septum and antenna. This energy dispersion increases with frequency, most likely due to a decrease of the conductivity due to high-frequency effects like the Skin-effect. Consequently, the power consumption in Figure 41 shows a square root relation to the frequency, because the power dispersion is so high. When changing the material of the antenna and septum to a perfect electric conductor, the total power in a system remains one (no power is dispersed) and the power consumption over frequency of the antenna shows a quadratic relation to the frequency, due to the quadratic increase of the radiation resistance.

The Skin-effect reduces the area in which the current flows, therefore increasing resistance. This appears due to the reduction of the depth, in which the electromagnetic waves enter. It is also called Skin depth and mathematically described by Equation 68b. It depends on the imaginary part of the wave number κ , which is described in Equation 68a. For high conducting materials ($\sigma \gg \epsilon\omega$), the dependency of the skin depth d on the frequency can be described therefore as $d \propto 1/\sqrt{\omega}$. Since the power dispersion is linearly proportional to the area of the conductor and therefore Skin-depth, it shows the same dependency on the frequency $P_{\text{disp}} \propto 1/\sqrt{\omega}$ [8].

Own little chapter for skin effect?

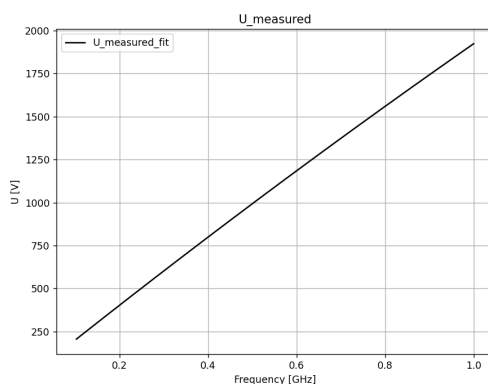


Figure 39: Voltage drop at feed point of current loop antenna

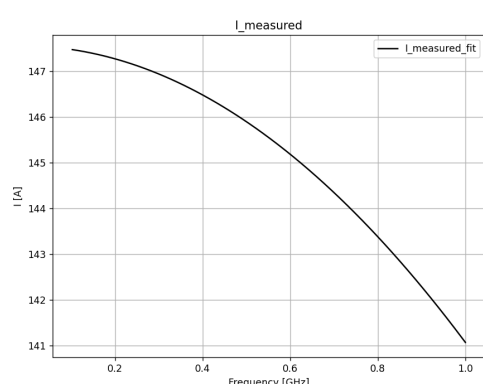


Figure 40: Current consumption at feed point of current loop antenna

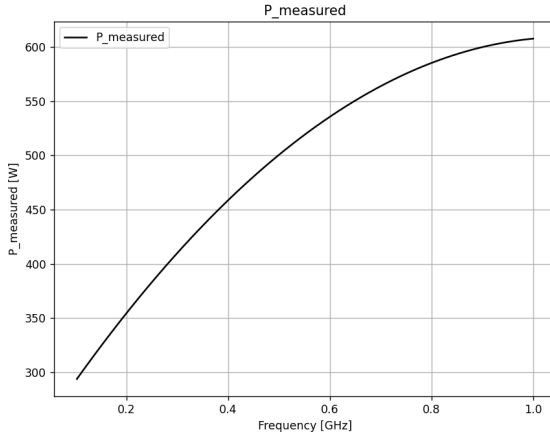


Figure 41: Power consumption of the current loop antenna

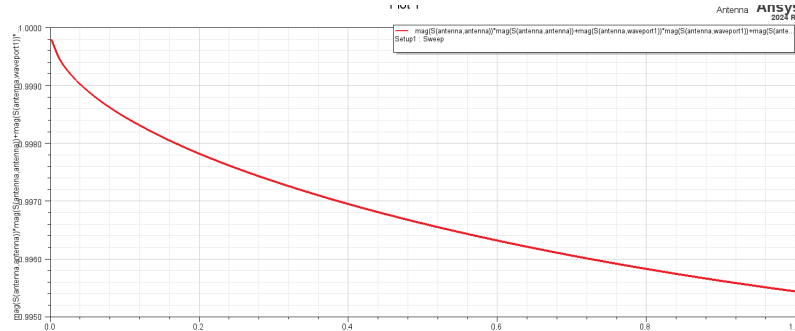


Figure 42: Total power distribution in the system

$$\kappa = \omega \sqrt{\frac{\epsilon \mu}{2}} \left[\sqrt{1 + \left(\frac{\sigma}{\epsilon \omega} \right)^2} - 1 \right]^{1/2} \quad (68a)$$

$$d = 1/\kappa \quad (68b)$$

At 1 GHz, the dispersed power already equals to 0.46 %, which is much higher than the power transfer of the antenna to one waveport of 1.26e-5 at that frequency. Because this dispersed power is proportional to the square-root of the frequency $P_{\text{disp}} \propto 1/\sqrt{\omega}$, the overall transferred power to the antenna shows the same characteristic. However, the power transfer to the waveports has a quadratic dependency on the frequency.

This dispersed power may be ignored in the simulations by changing the antenna's material (main source of power dissipation) and the septum from copper to a perfect electric conductor. The overall power in the system then remains at a constant one over the whole frequency range. Additionally, the transferred power to the antenna now has a quadratic relationship with the frequency, indicating increased radiation efficiency, previously described by Equation 9.

explain better.

The current-loop antenna contains two electric dipoles, shifted in phase by 180°. They

Show plots?

therefore oppose each other in the power transfer to the waveports. However, as visible in the electric near field plot in Figure 39, the electric dipole moment from node A to the feedpoint is much larger than the one from node B to ground. The reason can be demonstrated by representing the antenna with its nodes in ???. The partial inductances in this schematic are much larger than the capacitances. This leads to a large voltage drop between node A and B, and therefore a weaker electric dipole moment at node B.

Additionally, this voltage difference $V_A - V_B$ rises linearly over the frequency, due to the linearly increasing impedance of the inductance $i\omega L$. This means, that the over electric dipole moment a quadratic relationship to the frequency has.

4.1.5 Offset of source antennas and eddy currents

Next, the CFM is rotated by an angle. This angle is swept from 0° to 90° , iteratively increased by 1° [deg]. At 90° , it is already known that the magnetic dipole moment is zero, while it is the largest at 0° . The idea is now to find a balance between the electric and magnetic dipole moment, such that the antenna operates in a way of resonance. In this operation, the S11 parameter shall be the lowest, even though the coupling of the magnetic field only becomes weaker with increasing angle . The reason for this approach by increasing angle is that it is otherwise very hard to achieve such a balance between the dipole moments by purely scaling the antenna. The electric dipole moment is very weak, and when increasing the antenna height (thus only the electric dipole moment), it soon becomes very large and even touches the septum. Rotating the angle instead becomes a very efficient alternative. This has been determined just by looking at the phase shifts from the antenna to the waveports: If electric and magnetic dipole moments are roughly equally influential, then the phase shift between the ports shall be 90° . Very important for these simulation is the renormalization of the waveports . This enables the port exciting the antenna to have an impedance of 50 Ohm, independent of size. This will make a geometry sweep of the antenna able, without influencing the impedance of the port exciting the antenna (Imagine a coax cable attached to the antenna. It is hinted by the round waveport in the model. When it gets shifted around, its wave impedance changes, and so does the reflection, and the results are distorted)

Figure 43 it is visible, that the lowest S11 (least reflections) is achieved at a rotation angle of 72° .

Eddy currents occur on the septum. They increase with frequency. When they get too large, the next-order mode starts propagating. Offsetting the antenna / dipole moment in y-direction reduces the amount of influence of the eddy current on the power carrying current in the septum.

When implementing an offset in the center fed monopole antenna, the coupling between the waveports and the antenna changes. The change is visible in Figure 44, although the magnitude of the coupling to both ports is the same.

4.2 Dipole Moments

Magnetic moment equivalent antenna.
Explain with current and H-field, too

Prove square frequency dependency

Is it possible to proof this by mathematics?

Show mathematically?

Describe this in HFSS section, under excitations

Why, how do the dipole moments look like there?
Anf is this just a numerical error?

How does

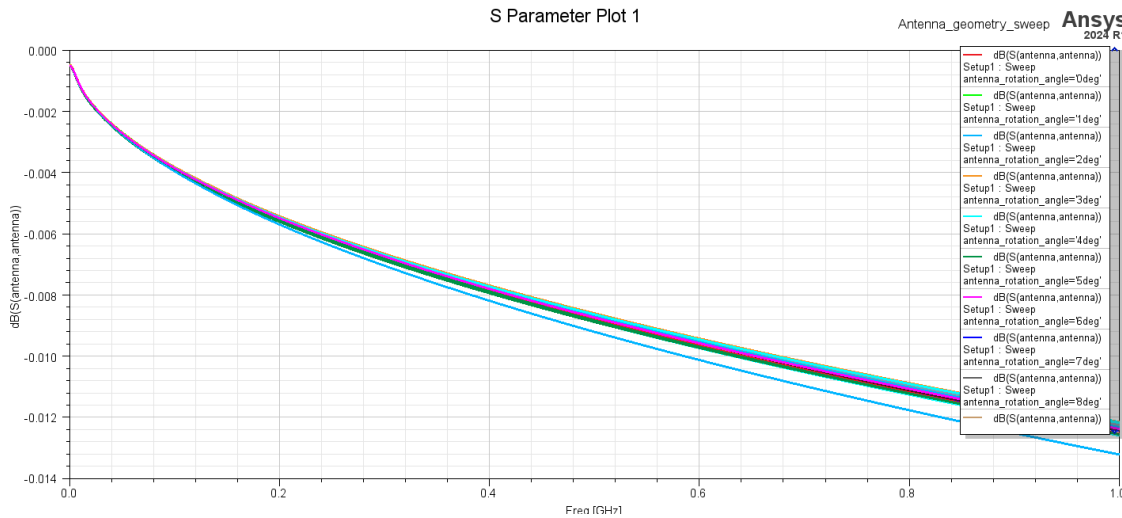


Figure 43: CFM S11 sweep with rotation angle stepping

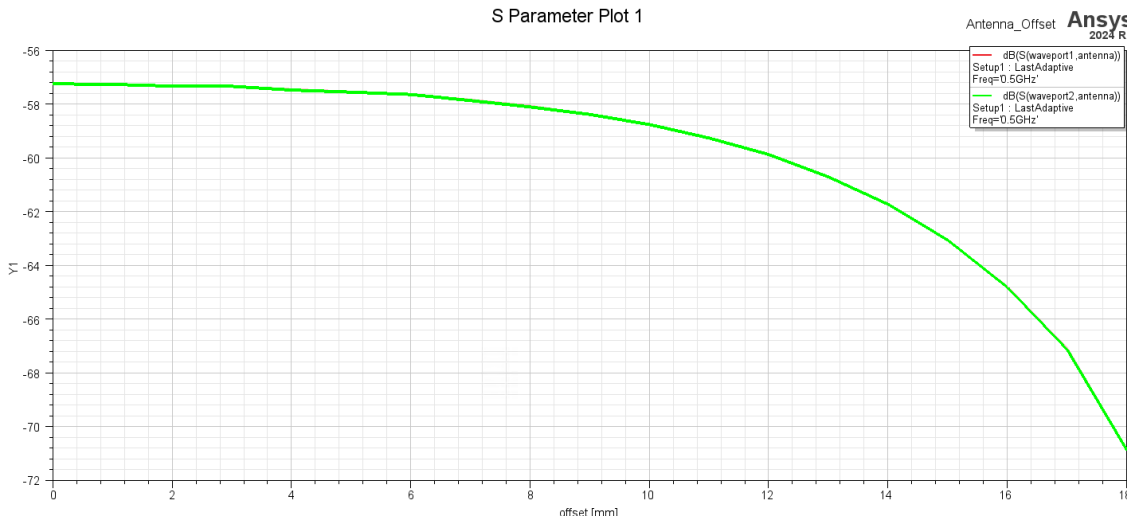


Figure 44: Center fed monopole antenna coupling dependence on offset (Delete after)

4.2.1 Orientation and position in TEM Cell

Figure 45 demonstrates the normalized output power of an electric dipole moment pointing in y-direction, and one in z-direction. This simulation only demonstrates the coupling behavior of the dipole moments over frequency, to explain the non-linear coupling of certain antennas. If dipole moments in certain positions and orientations couple with a different proportionality than the standard two dipole moments (e_z and m_y), then the non-linear coupling may be explained that way.

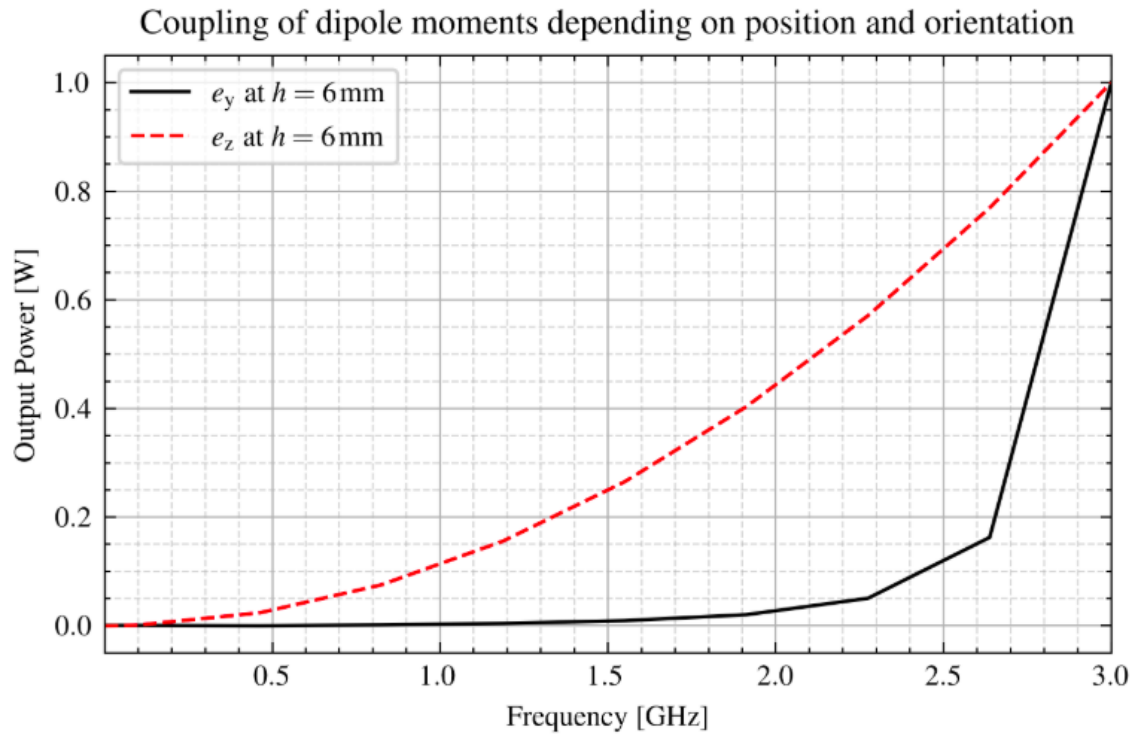


Figure 45: Comparison of normalized output power of electric dipole moments

The electric dipole moment in z-direction e_z demonstrates the expected behavior: As the frequency rises, this dipole moment rises linearly and thus increases the output power quadratically. The electric dipole moment in y-direction e_y also increases linearly with frequency, but does not significantly change the output power for the low frequencies. However, as the frequency approaches the cut-off frequency of the next-higher order mode, the coupling rises significantly.

This simulation is repeated where the dipole moments are located at a height of $h = 6\text{ mm}$, which is the dead center of the TEM cell, and $h = 9\text{ mm}$, which is near the top wall of the TEM cell. The simulation results are similar for both cases.

Repeat
Simula-
tion
for sev-
eral other
dipole
moment
positions
and orien-
tations?

4.2.2 Combining dipole moments with antennas

4.3 Shielding Simulations

4.3.1 Shielding effectiveness of graphite

The reference power P_{ref} has been set to 1 W. Using Equation 56 and the S-parameters from the simulation results, P_{load} may be determined. Figure 46 demonstrates the shielding effectiveness of graphite in dB SE_{dB} over the shielding material thickness. The solution frequency is 500 MHz. A frequency sweep shows that the reflection coefficient S_{11} does not depend much on the frequency.

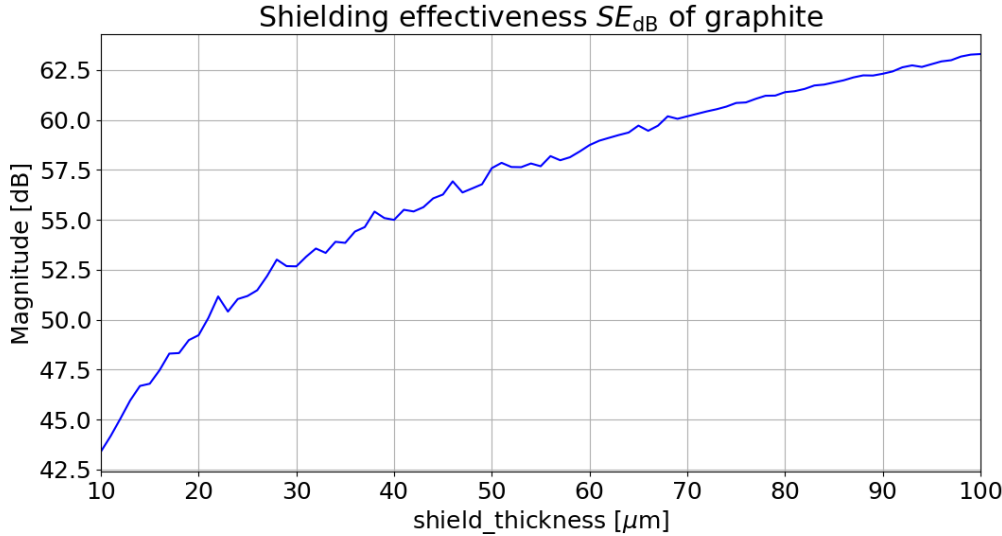


Figure 46: Shielding effectiveness of graphite

The components of SE_{dB} are determined according to Equation 47.

4.3.2 Shield effectiveness of FR4

The FR4 has a relative permittivity of $\epsilon_r = 4.4$. According to Equation 49, the relative wave impedance is $Z = 0.476$. This leads to a reflection coefficient of $R = -0.355$ by Equation 48.

The reflection coefficient $|S_{11}| = 0.045$.

4.3.3 Dual TEM Cell

A simulation setup of a dual TEM cell is created. A rectangular aperture with a side length of $l = 5 \text{ cm}$, inspired by [28], connects both TEM cells. One waveport 1, as in Figure 12, is excited with a power of $P = 1 \text{ W}$. The simulation is conducted, leaving the aperture open. A second one determines the coupling of the waveports, when the aperture is filled with a graphite sheet with a thickness of $t = 50 \mu \text{m}$.

I think the low SE in the low shield thicknesses has to do with the false modelling of it in Ansys HFSS.

Forward transmission coefficient	Empty aperture	aperture filled with FR408
Waveport 1 to 3 S_{13}	-83.80 dB, -144.96°	-85.27 dB, -155.79°
Waveport 1 to 4 S_{14}	-90.31 dB, -144.96°	-87.14 dB, 25.00°

Table 1: Forward transmission coefficients

At a frequency of $f = 500$ MHz, the coupling between waveport 1 to the waveports 3 and 4 of the receiving TEM cell is shown in Table 1. Only one frequency point is investigated, as the results stay roughly constant over the inspected frequency range from 100 MHz to 1 GHz.

Using Equation 57a and Equation 57b leads to the shielding effectiveness for electric coupling $SE_{dB}^e = 19.07$ dB and magnetic coupling $SE_{dB}^m = -9.22$ dB. To get the sum P_{sum} and difference P_{diff} of powers, the phase of the signals have to be considered. With unit input power at the transmitting TEM cell, Equation 69a and Equation 69b are used for this purpose [23].

$$P_{sum} = (S_{13} + S_{14})(S_{13} + S_{14})^* \quad (69a)$$

$$P_{diff} = (S_{13} - S_{14})(S_{13} - S_{14})^* \quad (69b)$$

Why -8dB difference in empty aperture?
Explained in [28]

negative SE possible?

Indicated by the phase shift of roughly 180°, the coupling between the TEM cells occur mainly due to magnetic dipoles. Due to the relative permittivity of $\epsilon_r = 3.66$ and the relative permeability of $\mu_r \approx 1$ of the shielding material, the magnetic fields dominate. This leads to a energy transfer mainly due to magnetic dipole moments. The overall shielding effectiveness $SE_{dB} =$ Equation 70.

$$P_{total} = |S_{13}|^2 + |S_{14}|^2 \quad (70)$$

One port receives overall more power due to the material. Is it because of the magnetic/electric dipoles in it?

Const antenna power definieren, damit dipolmomente einzelner antennen vergleichbar wird

References

- [1] Constantine A. Balanis. *Advanced Engineering Electromagnetics*. John Wiley Sons, 2012.
- [2] Constantine A. Balanis. *Antenna theory: Analysis and design. Buch Constantine A. Balanis*. 3rd. Wiley, 1997.
- [3] Z. Cendes and D. Shenton. “Adaptive mesh refinement in the finite element computation of magnetic fields”. In: *IEEE Transactions on Magnetics* 21.5 (1985), pp. 1811–1816. DOI: 10.1109/TMAG.1985.1063929.
- [4] Z.J. Cendes. “Vector finite elements for electromagnetic field computation”. In: *IEEE Transactions on Magnetics* 27.5 (1991), 3958–3966. DOI: 10.1109/20.104970.
- [5] Z.J. Cendes and J.-F. Lee. “The transfinite element method for modeling MMIC devices”. In: *1988., IEEE MTT-S International Microwave Symposium Digest* (1988), 623–626. DOI: 10.1109/mwsym.1988.22111.
- [6] Robert E. Collin. *Field theory of guided waves*. IEEE Press, 2015.
- [7] Saju Daniel and Sabu Thomas. “Shielding Efficiency Measuring Methods and Systems”. In: *Advanced Materials for Electromagnetic Shielding: Fundamentals, Properties, and Applications*. 2019, pp. 61–87. DOI: 10.1002/9781119128625.ch4.
- [8] David J. Griffiths. *Introduction to electrodynamics*. Cambridge University Press, 2024.
- [9] C. Groh et al. “TEM waveguides for EMC measurements”. In: *IEEE Transactions on Electromagnetic Compatibility* 41.4 (1999), pp. 440–445. DOI: 10.1109/15.809846.
- [10] K.H. Huebner et al. *The Finite Element Method for Engineers*. A Wiley-Interscience publication. Wiley, 2001. ISBN: 9780471370789. URL: <https://books.google.at/books?id=f3MZE1BYq3AC>.
- [11] John David Jackson. *Classical Electromagnetism*. 2nd ed. Wiley.
- [12] J.P. Karst, C. Groh, and H. Garbe. “Calculable field generation using TEM cells applied to the calibration of a novel E-field probe”. In: *IEEE Transactions on Electromagnetic Compatibility* 44.1 (2002), pp. 59–71. DOI: 10.1109/15.990711.
- [13] M. Koch, C. Groh, and H. Garbe. “Exact Determination of Resonant Frequencies in TEM Cells”. In: *13th International Zurich Symposium and Technical Exhibition on Electromagnetic Compatibility*. 1999, pp. 653–658. DOI: 10.23919/EMC.1999.10791592.
- [14] Galen H Koepke. In: *Theory and measurements of radiated emissions using a TEM cell* (1989). DOI: 10.6028/nist.tn.1326.
- [15] Dominik Kreindl et al. “Evaluation of an analytical equivalent Hertzian dipole representation in tem cells applying the finite element method”. In: *IEEE Transactions on Magnetics* 60.3 (2024), 1–4. DOI: 10.1109/tmag.2023.3324698.
- [16] Dominik Kreindl et al. “Fundamental investigation of wave propagation inside IC-striplines upon excitation with Hertzian dipole moments”. In: *Electronics* 11.16 (2022), p. 2488. DOI: 10.3390/electronics11162488.
- [17] J.-F. Lee, D.-K. Sun, and Z.J. Cendes. “Full-wave analysis of dielectric waveguides using tangential vector finite elements”. In: *IEEE Transactions on Microwave Theory and Techniques* 39.8 (1991), pp. 1262–1271. DOI: 10.1109/22.85399.

- [18] J.F. Lee, D.K. Sun, and Z.J. Cendes. “Tangential vector finite elements for electromagnetic field computation”. In: *IEEE Transactions on Magnetics* 27.5 (1991), pp. 4032–4035. DOI: [10.1109/20.104986](https://doi.org/10.1109/20.104986).
- [19] Paul Lorrain and Dale R. Corson. *Electromagnetic fields and waves*. W.H. Freeman, 1970.
- [20] M.F.N. Mohsen. “Some details of the Galerkin Finite Element Method”. In: *Applied Mathematical Modelling* 6.3 (1982), 165–170. DOI: [10.1016/0307-904x\(82\)90005-1](https://doi.org/10.1016/0307-904x(82)90005-1).
- [21] Cristian MORARI and Cristian BĂLAN. In: *Methods for determining shielding effectiveness of materials* (2015).
- [22] D. Shenton and Z. Cendes. “Three-dimensional finite element mesh generation using Delaunay tessellation”. In: *IEEE Transactions on Magnetics* 21.6 (1985), 2535–2538. DOI: [10.1109/tmag.1985.1064165](https://doi.org/10.1109/tmag.1985.1064165).
- [23] Ippalapalli Sreenivasah, David Chang, and Mark Ma. “Emission characteristics of electrically small radiating sources from tests inside a tem cell”. In: *IEEE Transactions on Electromagnetic Compatibility* EMC-23.3 (1981), 113–121. DOI: [10.1109/temc.1981.303930](https://doi.org/10.1109/temc.1981.303930).
- [24] GILBERT STRANG. *Analysis of the finite element method*. WELLESLEY-CAMBRIDGE Press, 2018.
- [25] Son Xuat Ta, Ikmo Park, and Richard W. Ziolkowski. “Crossed Dipole Antennas: A review”. In: *IEEE Antennas and Propagation Magazine* 57.5 (2015), pp. 107–122. DOI: [10.1109/MAP.2015.2470680](https://doi.org/10.1109/MAP.2015.2470680).
- [26] John C Tippet, David C Chang, and Myron L Crawford. In: *An analytical and experimental determination of the cutoff frequencies of higher-order te modes in a Tem cell* (1976). DOI: [10.6028/nbs.ir.76-841](https://doi.org/10.6028/nbs.ir.76-841).
- [27] C.M. Weil and L. Gruner. “High-order mode cutoff in rectangular striplines (short papers)”. In: *IEEE Transactions on Microwave Theory and Techniques* 32.6 (1984), 638–641. DOI: [10.1109/tmtt.1984.1132745](https://doi.org/10.1109/tmtt.1984.1132745).
- [28] Perry F Wilson. In: *Excitation of a tem cell by a vertical electric Hertzian dipole* (1981). DOI: [10.6028/nbs.tn.1037](https://doi.org/10.6028/nbs.tn.1037).
- [29] Perry F. Wilson, David C. Chang, and Mark T. Ma. “Input Impedance of a Probe Antenna in a TEM Cell”. In: *IEEE Transactions on Electromagnetic Compatibility* EMC-26.4 (1984), pp. 154–161. DOI: [10.1109/TEMC.1984.304216](https://doi.org/10.1109/TEMC.1984.304216).
- [30] Perry F. Wilson and Mark T. Ma. “Shielding-Effectiveness Measurements with a Dual TEM Cell”. In: *IEEE Transactions on Electromagnetic Compatibility* EMC-27.3 (1985), pp. 137–142. DOI: [10.1109/TEMC.1985.304277](https://doi.org/10.1109/TEMC.1985.304277).
- [31] Perry F. Wilson and Mark T. Ma. “Simple approximate expressions for higher order mode cutoff and resonant frequencies in TEM cells”. In: *IEEE Transactions on Electromagnetic Compatibility* 28.3 (1986), 125–130. DOI: [10.1109/temc.1986.4307269](https://doi.org/10.1109/temc.1986.4307269).